

The First Neptune Analog or Super-Earth with Neptune-like Orbit: MOA-2013-BLG-605Lb

T. Sumi^{1,2}, A. Udalski^{3,4}, D.P. Bennett^{5,6,2}, A. Gould⁷, R. Poleski^{3,4,7}, I.A. Bond^{8,2},
J.Skowron^{3,4}, N. Rattenbury^{9,2}, R. W. Pogge⁷, T. Bensby¹⁰, J.P. Beaulieu¹¹,
J.B. Marquette¹¹, V. Batista¹¹, S. Brillant¹²

and

F. Abe¹³, Y. Asakura¹³, A. Bhattacharya⁵, M. Donachie⁹, M. Freeman⁹, A. Fukui¹⁴,
Y. Hirao¹, Y. Itow¹³, N. Koshimoto¹, M.C.A. Li⁹, C.H. Ling⁸, K. Masuda¹³,
Y. Matsubara¹³, Y. Muraki¹³, M. Nagakane¹, K. Ohnishi¹⁵, H. Oyokawa¹³, To. Saito¹⁶,
A. Sharan⁹, D.J. Sullivan¹⁷, D. Suzuki⁵, P.,J. Tristram¹⁸, A. Yonehara¹⁹,

(The MOA Collaboration)

M.K. Szymański³, K. Ulaczyk³, S. Kozłowski³, Ł. Wyrzykowski³, M. Kubiak³, P.
Pietrukowicz³, G. Pietrzyński³, I. Soszyński³,

(The OGLE Collaboration)

and

C. Han²⁰, Y.-K. Jung²⁰, I.-G Shin²⁰, C-U. Lee²¹

ABSTRACT

We present the discovery of the first Neptune analog exoplanet or super-Earth with Neptune-like orbit, MOA-2013-BLG-605Lb. This planet has a mass

¹Department of Earth and Space Science, Graduate School of Science, Osaka University, Toyonaka, Osaka 560-0043, Japan,

e-mail: sumi@ess.sci.osaka-u.ac.jp

²Microensing Observations in Astrophysics (MOA)

³Warsaw University Observatory, Al. Ujazdowskie 4, 00-478 Warszawa, Poland; udalski, msz, mk, pietrzyn, soszynsk, szewczyk, kulaczyk@astrouw.edu.pl

⁴Optical Gravitational Lens Experiment (OGLE)

⁵Department of Physics, University of Notre Dame, Notre Dame, IN 46556, USA; bennett@nd.edu

⁶Laboratory for Exoplanets and Stellar Astrophysics, NASA/Goddard Space Flight Center, Greenbelt, MD 20771, USA

⁷Department of Astronomy, Ohio State University, 140 W. 18th Ave., Columbus, OH 43210, USA

⁸Institute of Information and Mathematical Sciences, Massey University, Private Bag 102-904, North Shore Mail Centre, Auckland, New Zealand; [i.a.bond](mailto:i.a.bond@massey.ac.nz), [c.h.ling](mailto:c.h.ling@massey.ac.nz), w.sweatman@massey.ac.nz

⁹Department of Physics, University of Auckland, Private Bag 92019, Auckland, New Zealand; n.rattenbury@auckland.ac.nz; p.yock@auckland.ac.nz; asha583@ucklanduni.ac.nz

¹⁰Lund Observatory, Department of Astronomy and Theoretical physics, Box 43, SE-221 00 Lund, Sweden

¹¹UPMC-CNRS, UMR7095, Institut d'Astrophysique de Paris, F-75014 Paris, France

¹²European Southern Observatory (ESO), Karl-Schwarzschildst. 2, D-85748 Garching, Germany

¹³ Institute for Space-Earth Environmental Research, Nagoya University, Nagoya 464-8601, Japan; abe@itow.kmasuda.ymatsu@stelab.nagoya-u.ac.jp

¹⁴Okayama Astrophysical Observatory, National Astronomical Observatory of Japan, 3037-5 Honjo, Kamogata, Asakuchi, Okayama 719-0232, Japan

¹⁵Nagano National College of Technology, Nagano 381-8550, Japan

¹⁶Tokyo Metropolitan College of Aeronautics, Tokyo 116-8523, Japan

¹⁷School of Chemical and Physical Sciences, Victoria University, Wellington, New Zealand

¹⁸Mt. John University Observatory, P.O. Box 56, Lake Tekapo 8770, New Zealand

¹⁹Department of Physics, Faculty of Science, Kyoto Sangyo University, 603-8555 Kyoto, Japan

²⁰Department of Physics, Institute for Astrophysics, Chungbuk National University, 371-763 Cheongju, Korea

²¹Korea Astronomy and Space Science Institute, 305-348 Daejeon, Korea

similar to that of Neptune or a super-Earth and it orbits at $9 \sim 14$ times the expected position of the snow-line, a_{snow} , which is similar to Neptune’s separation of $11 a_{\text{snow}}$ from the Sun. The planet/host-star mass ratio is $q = (3.6 \pm 0.7) \times 10^{-4}$ and the projected separation normalized by the Einstein radius is $s = 2.39 \pm 0.05$. There are three degenerate physical solutions and two of these are due to a new type of degeneracy in the microlensing parallax parameters, which we designate “the wide degeneracy”. The three models have (i) a Neptune-mass planet with a mass of $M_p = 21_{-7}^{+6} M_{\oplus}$ orbiting a low-mass M-dwarf with a mass of $M_h = 0.19_{-0.06}^{+0.05} M_{\odot}$, (ii) a mini-Neptune with $M_p = 7.9_{-1.2}^{+1.8} M_{\oplus}$ orbiting a brown dwarf host with $M_h = 0.068_{-0.011}^{+0.019} M_{\odot}$ and (iii) a super-Earth with $M_p = 3.2_{-0.3}^{+0.5} M_{\oplus}$ orbiting a low-mass brown dwarf host with $M_h = 0.025_{-0.004}^{+0.005} M_{\odot}$ which is slightly favored. The 3-D planet-host separations are $4.6_{-1.2}^{+4.7}$ AU, $2.1_{-0.2}^{+1.0}$ AU and $0.94_{-0.02}^{+0.67}$ AU, which are $8.9_{-1.4}^{+10.5}$, 12_{-1}^{+7} or 14_{-1}^{+11} times larger than a_{snow} for these models, respectively. The Keck AO observation confirm that the lens is faint. This discovery suggests that low-mass planets with Neptune-like orbit are common. So processes similar to the one that formed Neptune in our own Solar System or cold super-Earth may be common in other solar systems.

Subject headings: gravitational lensing: micro – planetary systems

1. Introduction

The formation of the ice giants Uranus and Neptune is not well understood. In the favored core accretion theory, the gas giant planets like Jupiter and Saturn are believed to form through the accumulation of small icy planetesimals into solid cores of about $5\text{--}15 M_{\oplus}$ in the region beyond the snow-line at $a_{\text{snow}} \approx 2.7(M_h/M_{\odot})$ (Ida & Lin 2004; Laughlin, Bodenheimer & Adams 2004; Kennedy, Kenyon & Bromley 2006), where the protoplanetary disk is cold enough for ices (especially water-ice) to condense. However, such a scenario is unable to form smaller ice giants like Uranus and Neptune at their current orbital positions, due to the low density of planetesimals and slow evolution in these orbits (Pollack et al. 1996). One idea is that Uranus and Neptune formed in the Jupiter-Saturn region between ~ 5 and ~ 17 AU, then migrated outwards to the current position (Fernandez 1984; Thommes, Duncan & Levison 1999; Helled & Bodenheimer 2013).

The formation of super-Earth exoplanets with Neptune-like orbit are even less understood. This is partly because we do not even know if they exist contrary to the case of Neptune. They are also not expected by the standard core accretion theory due to the same reason as that of ice giants mentioned above (Ida & Lin 2004). Their formation may be

similar to or related to the formation of Neptune-like ice giants.

The distribution of such cold ice-giant planets and super-Earth in other solar systems is important for understanding the formation of our own cold ice giants. Also, in our own Solar System, the distribution of Kuiper Belt objects (KBOs) is dominated by gravitational interactions with Neptune. Since KBOs hold large amounts of water and other volatiles needed for life, it could be that exo-neptunes play an important role in the development of life in some exoplanetary systems, whether or not they play this role in our own Solar System.

In the 20 years since the first exoplanet discovery (Mayor & Queloz 1995), there have been repeated discoveries of planets that are quite different from those in our own Solar System. However, the detection of planets similar to those in our own Solar System has been more difficult. Only Jupiter analogs have been detected orbiting solar type stars (Wittenmyer et al. 2014), while Jupiter/Saturn (Gaudi et al. 2008; Bennett et al. 2010) and Venus/Earth analogs (Burke et al. 2014; Quintana et al. 2014) have been found orbiting low-mass stars. Very cold, low-mass planets have yet to be explored (see the distribution of known exoplanets as of 2015 Oct. 6 ¹ in Figure 1). Cold ice-giants like Uranus and Neptune are very difficult to detect with the radial velocity and transit methods owing to their long orbital periods (80-160 years), low orbital velocities and low transit probabilities. It is even more difficult to detect a super-Earth in such wide orbit. The direct imaging method can detect wide-orbit planets if they are self-luminous, but otherwise, they will be far too faint to detect, especially if they are as small as Neptune and super-Earth.

Recently, low-mass stars (i.e. M-dwarfs) have attracted more interest in exoplanet search programs because of their high detectability of habitable or cold low-mass planets.

Kepler’s 150,000 targets contain about 3000 red dwarfs and more than a hundred planetary systems have been found orbiting these stars (Morton & Swift 2013). These results show that smaller planets are more common than larger planets around M-dwarfs, and planets with radii of $\sim 1.25 R_{\oplus}$ are the most common planets in these systems. Dressing & Charbonneau (2013) estimated an occurrence rate of ~ 0.5 habitable zone Earth size planets per M-dwarf, and Quintana et al. (2014) found an Earth-radius habitable planet around a $\sim 0.5 M_{\odot}$ M-dwarf. That smaller planets are more common than larger planets around M-dwarfs may be related to the fact that only small mass proto-planetary disks have been found around such low mass stars (Kennedy & Kenyon 2008). The TRENDS high-contrast imaging survey, in combination with radial velocity measurements, indicates that $6.5\% \pm 3.0\%$ of M-dwarf stars host one or more massive companions with $1 < m/M_J < 13$ and $0 < a < 20$ AU, however

¹<http://exoplanet.eu>

this survey is not sensitive to cold ice planets (Montet et al. 2014; Clanton & Gaudi 2014).

The gravitational microlensing method is also sensitive to planets around M-dwarfs and even brown dwarfs because it does not rely on the light from the host stars. Microlensing relies upon random alignments between background source stars and foreground lens star+planet systems, and more massive lens stars are only favored by the factor \sqrt{M} while smaller masses have shorter timescales which can also bias against detection. So M-dwarf lens stars dominate microlensing events. Contrary to the other methods, microlensing is sensitive to low-mass planets down to an Earth-mass (Bennett & Rhie 1996) orbiting beyond the snow-line, as shown in Fig. 1. Microlensing is therefore complementary to the other planet detection techniques. Statistical analyses of microlensing samples indicate that the planet abundance beyond the snow line is about a factor ~ 7 larger than the abundance of close-in planets. Neptune mass planets are more abundant than gas giants around M-dwarfs, and one or more planets per star in total are predicted just beyond the snow-line (Sumi et al. 2010; Gould et al. 2010; Cassan et al. 2012).

In about half of the planetary systems found by microlensing, the mass of the host and planets and their projected separation have been measured by microlensing parallax in combination with the finite source effect (Bennett et al. 2008; Gaudi et al. 2008; Muraki et al. 2011; Kains et al. 2013; Tsapras et al. 2014; Udalski et al. 2015) and/or direct detection of the lens flux by high resolution imaging by adaptive optics (AO) (Bennett et al. 2010; Kubas et al. 2012; Batista et al. 2014, 2015) or the *Hubble Space Telescope* (*HST*) (Bennett et al. 2006, 2015; Dong et al. 2009b). The probability distribution of physical mass and separations of other events have been estimated using a Bayesian analysis assuming a Galactic model. Among the planetary systems with mass measurements, two of them have very low mass hosts, less than $0.2M_{\odot}$ and each system has a planetary mass ratio $q < 0.01$. These two systems are MOA-2007-BLG-192L ($M_h = 0.084^{+0.015}_{-0.012}M_{\odot}$, $M_p = 3.2^{+5.2}_{-1.8}M_{\oplus}$) (Bennett et al. 2008; Kubas et al. 2012) and MOA-2010-BLG-328L ($M_h = 0.11 \pm 0.01M_{\odot}$, $M_p = 9.2 \pm 2.2M_{\oplus}$) (Furusawa et al. 2013). Neptune analog planets and super-Earth with Neptune-like orbit are still difficult to detect even by microlensing.

Recently, Poleski et al. (2014) found a planet in a Uranus-like orbit with mass of $\sim 4 M_{\text{Uranus}}$ at ~ 18 AU around $\sim 0.7 M_{\odot}$ star. This is ~ 9 times the snow-line of the host. While their mass estimates are based on a Bayesian analysis and have large uncertainties, their detection demonstrated the ability to detect planets in these orbits with microlensing.

In this paper, we present the detection and the mass measurement of the first Neptune analog MOA-2013-BLG-605Lb via microlensing. We detected the microlensing parallax effect which yield the mass measurement of the lens system in combination with the finite source effect.

Microensing parallax can be measured when one observes an event simultaneously from two different locations, either with a telescope on Earth and a space telescope, (Refsdal 1966; Udalski et al. 2015) or with two ground-based telescopes, referred to as terrestrial parallax (Gould et al. 2009). It is known that there is a four-fold degeneracy in these parallax measurements, (Refsdal 1966; Gould 1994). Two elements of this four-fold degeneracy correspond to two different magnitudes of the measured parallax. As a result, the physical parameters of the lens differs between these two degenerate solutions. The other two degenerate solutions in the four-fold degeneracy just arise from a symmetry in the lensing geometry. The physical parameters of the lens are the same between these two degenerate solutions, except the projected velocities which can be used to distinguish among solutions (Calchi Novati et al. 2015a). Most commonly, parallax measurements have been made by observing an event from an accelerated observatory; specifically from ground-based observations of an event which is long enough for Earth to move significantly in its orbit around the Sun. This is referred to as orbital parallax (Gould 1992). There is also an analogous four-fold discrete degeneracy for orbital parallax, termed the “jerk parallax” degeneracy and their mirror solutions (Gould 2004; Park et al. 2004). For the binary lens case, there is an approximate degeneracy in the parallax parameters, known as the “ecliptic degeneracy” (Skowron et al. 2011). In this work on event MOA-2013-BLG-605, we report a new type of degeneracy in parallax model solutions, which is specific to widely separated binary lenses. The details of this new degeneracy are presented in section § 4.

We describe the observations of, and photometric data for, event MOA-2013-BLG-605 in sections § 2 and § 3. The light curve modeling is described in section § 4. In section § 5 and § 6 we present the physical parameters of the lens system and constraints by the Keck AO observation. We discuss, in section § 7, the manner in which we might measure the lens mass in the future and we present an overall discussion and our conclusions in section § 8.

2. Observation

The Microlensing Observations in Astrophysics (MOA; Bond et al. 2001; Sumi et al. 2003) collaboration carries out a microlensing survey toward the Galactic bulge from the Mt. John University Observatory in New Zealand. The MOA-II survey (Sumi et al. 2011) is a very high cadence photometric survey of the Galactic bulge with the 1.8m MOA-II telescope equipped with a 2.2 deg^2 field-of-view (FOV) CCD camera. The 2013 MOA-II observing strategy called for the 6 fields ($\sim 13 \text{ deg}^2$) with the highest lensing rate to be observed with a 15 minute cadence, while the next 6 best fields were observed with a 47 minute cadence, and 8 additional fields were observed with a 95 minutes cadence. Most

MOA-II observations use the custom MOA-red wide band filter, which corresponds to the sum of the standard Cousins R and I -bands. MOA-II issues ~ 600 alerts of microlensing events in real time each year.²

The Optical Gravitational Lensing Experiment (OGLE; Udalski, Szymański and Szymański 2015) also conducts a microlensing survey toward the Galactic bulge with the 1.3 m Warsaw telescope at the Las Campanas Observatory in Chile. The fourth phase of OGLE, OGLE-IV started its high cadence survey observations in 2010 with a 1.4 deg^2 FOV mosaic CCD camera. OGLE observes bulge fields with cadences ranging from one observation every 20 minutes for 3 central fields to less than one observation every night for the outer bulge fields. Most observations are taken in the standard Kron-Cousin I -band with occasional observations in the Johnson V -band. OGLE-IV issues ~ 2000 microlensing event alerts in real time each year.³

The microlensing event MOA-2013-BLG-605 was discovered at $(\alpha, \delta)(2000) = (17:58:42.85, -29:23:53.66)$ $[(l, b) = (1.0583^\circ, -2.695^\circ)]$, in MOA field gb9, which is monitored every 15 min, and it was announced by the MOA Alert System on 2013 Aug 30 ($\text{HJD}' \equiv \text{HJD} - 2450000 \sim 6535$). Figure 2 shows the light curve. At the time of its discovery, MOA recognized this event as a possible free-floating planet candidate (Sumi et al. 2011) as the best fit single lens light curve had an Einstein radius crossing time of $t_E = 0.73 \pm 0.10$ days (See Figure 2). Nearly four weeks later, the OGLE Early Warning System (EWS) (Udalski 2003) detected this event being magnified again with longer timescale due to the lensing effect of the host star. The OGLE EWS system announced this event as OGLE-2013-BLG-1835 on 2013 Sep 25 ($\text{HJD}' \sim 6560$), as shown in the top panel of Figure 2. The initial short magnification by the planet at $\text{HJD}' \sim 6535$ was confined by the OGLE survey data. Actually, it should have triggered the OGLE discovery alert but due to unfortunate deeply hidden bug in the EWS software this did not happen. The later magnification by the host was observed by MOA, as well as OGLE.

Follow-up observations of the stellar part of the light curve in the V , I and H -bands were obtained by the μFUN collaboration using the SMARTS-CTIO 1.3 m telescope. These data were taken mainly to extract the source color. We use the average of these CTIO and OGLE $V - I$ color measurements. CTIO H -band measurements are used to drive H -band source magnitude, which is very important for comparison to the AO observations (see Section 6).

²<https://it019909.massey.ac.nz/moa/>

³<http://ogle.astrouw.edu.pl/ogle4/ews/ews.html>

3. Data Reduction

The MOA images were reduced with MOA’s implementation (Bond et al. 2001) of the difference image analysis (DIA) method (Tomany & Crotts 1996; Alard & Lupton 1998; Alard 2000). In the MOA photometry, we found that there were systematic errors that correlate with the seeing and airmass, as well as the motion, due to differential refraction, of a nearby, possibly unresolved star. There is also a potential systematic error due to the relative proper motion of a nearby star or stars, which we model as linear function in time. We ran a detrending code to measure these effects in the 2011, 2012 and 2014 data, and we removed these trends with additive corrections to the full 2011-2014 data set. (The MOA data from 2006-2010 indicate no significant photometric variations, but they are not included in the light curve analysis.) This detrending procedure improved the fit χ^2 by $\Delta\chi^2 = 0.073$ per data point in the baseline, so it has reduced the systematic photometry errors significantly. This investigation of the systematics is necessary to have confidence in the modeling of the light curve with high order effects in the following section.

The OGLE data were reduced with the OGLE DIA (Woźniak 2000) photometry pipeline (Udalski, Szymański and Szymański 2015). In this event, the center of the magnified source star is slightly shifted from the center of the apparent star identified in the reference image, due to blending with one or more unresolved stars. So the OGLE data have been re-reduced with a centroid based difference images, just as the MOA pipeline does (Bond et al. 2001).

The number of data points used for the light curve modeling are 9675, 5514 and 64 for MOA-Red, OGLE-*I* and OGLE-*V* passbands, respectively. The photometric errorbars provided by the photometry codes give approximate estimates of the absolute photometric uncertainty of each measurement, and we regard them as an accurate representation of the relative uncertainty for each measurement. This is adequate for determining the best light curve model, but in order to determine the uncertainties on the model parameters, it is important to have more accurate error bars. We accomplish this with the method presented in Yee et al. (2012). We rescale the errors using the formula, $\sigma'_i = k\sqrt{\sigma_i^2 + e_{\min}^2}$, where σ_i and σ'_i are original and renormalized errorbars in magnitudes. The parameters k and e_{\min} are selected so that the cumulative χ^2 distribution sorted by the magnification of the best model is a straight line of slope 1 and $\chi^2/\text{dof} \sim 1$. This procedure yields $k = 1.092313$ and $e_{\min} = 0.012662$ for MOA-Red, $k = 1.387059$ and $e_{\min} = 0.010938$ for OGLE-*I* and $k = 1.571492$ and $e_{\min} = 0.0$ for OGLE-*V*. Note that the changes of the final best fit model due to this error renormalization are negligible.

CTIO data were reduced by DoPHOT (Schechter, Mateo & Saha 1993), the point spread function (PSF)-fitting routine. The number of data points in the CTIO-*I*, *V* and *H* passbands is 15, 15 and 149, respectively. Their error bars are not rescaled, i.e., $k = 1.0$ and

$e_{\min} = 0.0$. These CTIO data are not used for light curve modeling, but used for obtaining the source color in $(V - I)$ and $(I - H)$ in a model-independent way from the linear regression of these light curves by following Dong et al. (2009a) and Calchi Novati et al. (2015b).

Details of the datasets are summarized in Table 1.

4. Light curve modeling

We search for the best fit models of the standard (static), the parallax, the parallax with the linear orbital motion of the planet, the keplerian orbital motion, with the keplerian prior, the Galactic kinematic constraint and the Galactic density prior using Markov Chain Monte Carlos (MCMC) (Verde et al. 2003). The best fit models are shown in Table 2-7 and their physical parameters are in Tables 8-13, respectively (see Section 5).

4.1. Standard (static) model

In a point-source point-lens (PSPL) microlensing model, there are three parameters, the time of peak magnification t_0 , the Einstein radius crossing time t_E , and the minimum impact parameter u_0 . The standard binary lens model has four more parameters, the planet-host star mass ratio q , the projected separation normalized by Einstein Radius s , the angle of the source trajectory relative to the binary lens axis α , and the ratio of the angular source radius to the angler Einstein radius $\rho = \theta_*/\theta_E$. ρ can only be measured for events that show finite source effects. The measurement of ρ is important because it allows us to determine the angular Einstein radius $\theta_E = \theta_*/\rho$ since the angular source radius, θ_* , can be estimated from its color and extinction-corrected apparent magnitude (Kervella et al. 2004).

We use linear limb-darkening models for the source star using the coefficients, $u = 0.5863, 0.7585$ and 0.6327 for the I , V and MOA-Red bands, respectively (Claret 2000). The MOA-Red value is the mean of the R and I -band values. These values were selected from Claret (2000) for a K2 type source star with $T = 5000$ K, $\log g = 4.0$ and $\log[M/H] = 0$, based on the extinction corrected, best fit source $V - I$ color and brightness (see Section 5).

Initially, the global grid search of the best fit model was conducted with 9,680 fixed grid points across a wide range of three parameters, $-4.0 < \log q < 0.4$, $-0.5 < \log s < 0.6$ and $0 < \alpha < 2\pi$, with all other parameters being free. Then the most likely models were refined, allowing all parameters to vary. Using this robust search methodology, we avoid missing any local minimum solutions across the wide range of parameter space. We found that only the model with a wide separation ($s > 1$) reproduces the observed light curve data. The model

corresponds to the source crossing a planetary caustic. Planetary caustics can form far from the primary and any source star that crosses or passes close to such a distant a planetary caustic will impose an signal far from the main microlensing peak. Furthermore, the shape of planetary caustics differ significantly between wide ($s > 1$) and close ($s < 1$) configurations in contrast to the close/wide degeneracy for an event crossing a central caustic near the primary. The best fit standard model parameters are shown in Table 2. The mass ratio of $q \sim 3 \times 10^{-4}$ and separation of $s \sim 2.3$ indicate that the companion is a relatively low mass planet at wide separation.

The single lens model with a binary source was ruled out as follows. We extracted 88 data points around the planetary anomaly within $6533.0 < \text{HJD}' < 6536.6$ after subtracting the flux contribution from the best fit single lens model of the primary peak which is fitted without data around the anomaly. We fitted this extracted light curve by the single lens model with a finite source effect. The best fit χ^2 is ~ 31 larger than the χ^2 contributions from the same data points by the planetary models with parallax and orbital motion K_{pk} (see §4.4.3). Furthermore, the best fit event timescale of $t_E = 2.3$ days is much smaller than $t_E \sim 20$ days of the main peak, while they should be same if a single lens caused both two magnifications.

4.2. Parallax model with a New Type of Degeneracy

There are higher order effects that require additional parameters. The orbital motion of the Earth can cause the apparent lens-source relative motion to deviate from a constant velocity. This effect is known as the microlensing parallax effect (Gould 1992; Alcock et al. 1995; Smith, Mao & Woźniak 2002), and it can be described by the microlensing parallax vector $\boldsymbol{\pi}_E = (\pi_{E,N}, \pi_{E,E})$. The direction of $\boldsymbol{\pi}_E$ is the direction of the lens-source relative motion projected on the sky (geocentric proper motion at a fixed time), and the amplitude of the microlensing parallax vector, $\pi_E = \text{AU}/\tilde{r}_E$, is the inverse of the Einstein radius, projected to the observer plane. Because the Galactic bulge is close to the ecliptic plane, there is an approximate degeneracy in the parallax parameters, known as the “ecliptic degeneracy,” where models with similar parameters but with $(u_0, \alpha, \pi_{E,N}) = -(u_0, \alpha, \pi_{E,N})$ produce nearly indistinguishable light curves. This corresponds to a reflection of the lens plane with respect to the geometry of Earth’s orbit, (Smith, Mao & Paczyński 2003; Skowron et al. 2011).

We found the four degenerate parallax models as shown in Table 2. The light curves of these four models are almost identical to the one shown in Figure 2. The caustics, critical curves and source trajectory of these models are shown in Figure 3. The “P” scripts indicate models with microlensing parallax. The “+” and “−” subscripts refer to two different 2-

fold degeneracies in the parallax models. The first “ \pm ” subscript refers to the sign of the u_0 parameter, and refers to the “ecliptic degeneracy” mentioned above, but the second “ \pm ” subscript refers to a new parallax degeneracy, the wide degeneracy, that is particular to events like this, with a wide separation planet detected through a crossing of the planetary caustic. The light curve measurements indicate the angle, $\alpha(t_{\text{pcc}})$, between the source trajectory and lens axis at the time of the planetary caustic crossing, t_{pcc} . Due to the reflection symmetry of the lens system, the light curve constrains $\alpha(t_{\text{pcc}})$ up to a reflection symmetry, as shown in Figure 3. If there were no microlensing parallax, we could use $\alpha(t_{\text{pcc}})$ to predict the closest approach of the source to the center-of-mass, u_0 , and therefore the peak magnification of the the stellar part of the microlensing light curve. But, when the microlensing parallax effect is included, the angle α can vary in time, so that $\alpha(t_{\text{pcc}}) \neq \alpha(t_0)$. For a wide-separation planetary event, like MOA-2013-BLG-605, the light curve basically constrains the microlensing parallax through the three parameters, $\alpha(t_{\text{pcc}})$, u_0 , and t_0 , which is essentially the time of the stellar peak magnification (cf. An & Gould 2001). As a result, the configurations shown in the upper and lower panels of Figure 3 yield nearly identical light curves as shown in Figure 2, even though the source passes through in between the two masses in the upper panels and below or above the masses in the bottom two panels. The lower panels imply a larger curvature of the source trajectory, and therefore, a larger microlensing parallax signal. (Note that the model parameter α_0 and s_0 given in Table 2-7 are the α and s values at a fixed time $t_{\text{fix}} = 6573.045$, following the convention of Geocentric microlensing parallax parameters.)

Fig. 4 shows the $\Delta\chi^2$ distribution of the parallax parameters from the best fit MCMC models. The best fit values are compared to that of other models in Figure 6. In late September, the Earth’s acceleration is in the East-West (E-W) direction, so for a typical event, we would expect a better constraint on parallax in the E-W direction, i.e, a smaller error for $\pi_{\text{E,W}}$. However, in this case, the planetary signal plays a big role in the parallax signal. The angle and timing of caustic entry for a given u_0 value – which is constrained by the main peak corresponding to the host star – constrain the parallax parameters.

Figure 5 shows the difference in the cumulative χ^2 values between the standard and the parallax models as a function of time. We can see that most of the parallax signals come from around the planetary signal in both MOA-Red and OGLE-*I* as expected.

For all these models, q and s are similar to that of the standard model, so the companion is a cold low mass planet. For all 4 degenerate solutions, the model parameters of greatest interest are all very similar, except for the microlensing parallax. The ecliptic degeneracy yields nearly identical physical parameters, except that the direction of the lens-source relative motion is different. Potentially, this angle can be measured with follow-up observations (Bennett et al. 2015; Batista et al. 2015). In contrast to the ecliptic degeneracy, the wide de-

generacy implies different amplitudes, π_E , of the microlensing parallax vector, which implies different lens system masses, as discussed in Section 5 below.

Thus, this wide degeneracy presents us with two different classes of physical models, $P_{\pm\mp}$ and $P_{\pm\pm}$, where the $P_{\pm\pm}$ models have larger π_E implying smaller lens system masses and distance (see Section 5 and Table 8).

These four parallax models are preferred over the standard $\pi_E = 0$ model in both the MOA-Red and OGLE-*I* bands by $(\Delta\chi^2_{\text{MOA}}, \Delta\chi^2_{\text{OGLE}}) = (-21.8, -11.5)$, $(-21.6, -11.1)$, $(-21.9, -12.5)$ and $(-23.6, -12.8)$ for the P_{+-} , P_{-+} , P_{++} and P_{--} models, respectively. In total, the χ^2 differences range from $\Delta\chi^2 = -33.3$ to -37.1 . In Figure 5, one can also see that these χ^2 improvements came from the same region of the light curves around the planetary anomaly in both datasets. Microlensing parallax signals can sometimes be mimicked by the systematic errors in the light curve photometry, but a consistent signal seen in both the MOA and OGLE data implies that the signal is likely to be real.

4.3. Xallarap model

The xallarap effect is a light curve distortion caused by the orbital motion of the source star (Griest & Hu 1992; Han & Gould 1997), so it only occurs if the source star has a binary companion (Derue et al. 1999; Alcock et al. 2001). Xallarap can be represented by five additional model parameters. The xallarap vector $\xi_E = (\xi_{E,N}, \xi_{E,E})$ is similar to the parallax vector, π_E , and represents the direction of the lens-source relative motion. The amplitude of the xallarap vector, $\xi_E = a_s/\hat{r}_E$ is the semimajor axis of the source’s orbit, a_s , in units of the Einstein radius projected on the source plane, $\hat{r}_E = \theta_E D_s$. The other xallarap parameters are the direction of the observer relative to the source orbital axis, with vector components $R.A._\xi$ and $decl._\xi$, and the source binary orbital period, T_ξ . For an elliptical orbit, two additional parameters are required, the orbital eccentricity, ϵ and time of perihelion, t_{peri} , which we did not consider here as their inclusion did not improve the fit of the model to the data.

We found xallarap models giving only marginally better χ^2 values compared to parallax models for $T_\xi \geq 160$ days and worse values of χ^2 for shorter values of T_ξ . This is not surprising as it is known that xallarap effects can mimic parallax effects (Smith, Mao & Paczyński 2003; Dong et al. 2009a). Including xallarap yields a slight improvement of $\Delta\chi^2 \sim -5$ for $160 \leq T_\xi < 200$ days and $\Delta\chi^2 \sim -9$ at $T_\xi \geq 200$ days. However, these models lead to a xallarap amplitude of $\xi_E \geq 0.26$, which is larger than would be induced by a “normal”

main-sequence companion. Here ξ_E is expressed, making use of Kepler’s third law, by

$$\xi_E = \frac{a_s}{\hat{r}_E} = \frac{1\text{AU}}{\hat{r}_E} \left(\frac{M_c}{M_\odot} \right) \left(\frac{M_\odot}{M_c + M_s} \frac{T_\xi}{1\text{yr}} \right)^{\frac{2}{3}}. \quad (1)$$

These models require a source companion of mass $M_c > 6M_\odot$ for $T_\xi \geq 160$ days and $M_c > 40M_\odot$ for $T_\xi \geq 200$ days. Such a heavy object would most likely be a stellar remnant or a black hole – in either case, a rare object and thus an unlikely source companion. For this reason we reject the inclusion of the xallarap in our models.

4.4. Orbital motion model

4.4.1. Linear Orbital Motion

The orbital motion of the planet around the host star causes a similar effect as parallax. To a first-order approximation, the orbital motion of the planet is described by two parameters, the rate of change, $\omega = d\alpha/dt$ (radian yr^{-1}), of the binary axis angle α , and the rate of change ds/dt (yr^{-1}), of the projected lens star and planet separation s (Dong et al. 2009a; Batista et al. 2011), as follows,

$$s = s_0 + ds/dt(t - t_{\text{fix}}), \quad \alpha = \alpha_0 + \omega(t - t_{\text{fix}}), \quad (2)$$

where, s_0 and α_0 are instantaneous value of s and α at the time t_{fix} . We required the planet to be bound. That is, the ratio of the projected kinetic energy and potential energy,

$$\left(\frac{\text{KE}}{\text{PE}} \right)_\perp = \frac{(r_\perp/\text{AU})^3}{8\pi^2(M/M_\odot)} \left[\left(\frac{1}{s} \frac{ds}{dt} \right)^2 + \left(\frac{d\alpha}{dt} \right)^2 \right] \text{yr}^2, \quad (3)$$

which is less than the ratio of kinetic to potential energy (KE/PE) in three dimensions, was required to be less than unity in the MCMC calculations used to determine the model parameter distributions. The four best linear orbital motion models (with scripts ”L”) that correspond to each of four parallax models in Table 2, are shown in Table 3. One finds that π_E and its uncertainty significantly increased, while the χ^2 only slightly improved. This is because of the well known degeneracy between one component of the parallax vector, $\pi_{E,\perp}$, which is the perpendicular to the binary axis and close to $\pi_{E,N}$ in this case, and the lens orbital rotation on the sky, ω . As an example, $\Delta\chi^2$ distribution of $\pi_{E,N}$ and ω for the model $P_{+-}L$ is shown in Figure 7.

Note that there are two additional degenerate models $P_{\pm\pm}L'$ which have smaller $s_0 \sim 1.97$ and larger $ds/dt \sim -4.1 \text{ yr}^{-1}$ compared to the other models. Here, s of these models

are similar to others, $s \sim 2.4$, when the source crosses the planetary caustic. However these models are disfavored with the full Keplerian orbit in the following analysis.

The physical parameters of the lens system of these models are shown in Table 9 (see details in section §5). The host stars in these four models have a brown dwarf mass. Note that $(\text{KE/PE})_{\perp}$ of these models given in Table 9 are close to unity. The probability of having such high value is quite low as it requires very large eccentricity of $e \sim 1$, seeing the orbital plane face-on. If the parameters are not well constrained by the light curve, the density distribution of the MCMC chain depends on the prior probability of the fitting parameters in MCMC. Although the linear approximation of the lens motion is good enough in most of the cases, this parameterization inadvertently assumed the uniform prior on all microlensing fitting parameters, which is not physically justified. We need to use a full keplerian orbit parameterization to introduce physically justified priors.

4.4.2. Full Keplerian Orbit

To take the proper weighting on the orbital parameters, we adopt the full Keplerian parameterization by Skowron et al. (2011). The advantage of the full Keplerian orbit is not only being more accurate and allowing only bound orbital solutions, it also enables us to introduce physically justified priors on the orbital parameters. In addition to the parameters defined above, we introduce the position and velocity along the line of sight, s_z in units of r_E and ds_z/dt in yr^{-1} . Then, the three dimensional position and velocity of the secondary relative to its host can be described by $(s_0, 0, s_z)$ and $s_0(\gamma_{\parallel}, \gamma_{\perp}, \gamma_z) = (ds/dt, s_0\omega, ds_z/dt)$.

We run MCMC fitting using the microlensing parameters with these six instantaneous Cartesian phase-space coordinates, in which we transform the “microlensing” parameters to “Keplerian” parameters, i.e., eccentricity (e), time of periapsis (t_{peri}), semi-major axis (a) and three Euler angles, longitude of the ascending node (Ω_{node}), inclination (i), and argument of periapsis (ω_{peri}). By following Skowron et al. (2011), we assume flat priors on values of eccentricity, time of periapsis, $\log(a)$, and ω_{peri} . Owing to the fact that orbital orientation is random in space, we multiply the prior by $|\sin i|$. We must multiply the Jacobian of the parameter transformation function, $j_{\text{kep}} = |\partial(e, a, t_{\text{peri}}, \Omega_{\text{node}}, i, \omega_{\text{peri}})/\partial(s_0, \alpha_0, s_z, \gamma_{\parallel}, \gamma_{\perp}, \gamma_z)|$ (Eq. B6 in Skowron et al. 2011). So we adopt the Keplerian orbit prior of $P_{\text{kep}} = j_{\text{kep}} |\sin i| a^{-1}$ and added the $\Delta\chi^2$ penalty of $\Delta\chi_{\text{kep}}^2 = -2 \ln(P_{\text{kep}})$.

We first show the results with full Keplerian orbit (with scripts “K”) without any priors in Table 4 and Table 10. The results are almost same as the ones with the linear approximation of the orbit. The large eccentricity of $e \sim 1$ seeing the orbital plane face-on

($i \sim 0, 180^\circ$) is as expected from the large $(\text{KE}/\text{PE})_\perp$ in the linear orbit. The physical parameter of the keplerian orbits, semi-major axis a_{kep} , period P , e , and i are not well constrained so that they have very large asymmetric error bars in MCMC in Table 10. Here, when the best fit is larger or smaller than the 68% confidence interval of MCMC chains, the upper or lower limit is designated as “+0.0” or “−0.0”, respectively. So the light curve shape itself does not constrain the parameters more than the linear orbit model, except that it ruled out the models with smaller s_0 and larger ds/dt corresponding to $P_{\pm\pm}L'$. The best fit parallax vectors are larger than that of the static model as shown in Figure 6. Note that, the ratio of 3D kinetic to potential energy (KE/PE) can be calculated in these full Keplerian orbit models as shown in Table 10. which are also close to unity.

The results with the Keplerian orbit with the Keplerian prior (with scripts “K_p”) are shown in Table 5, Table 11 and Figure 6. With the Keplerian prior, the circular orbits with $e \sim 0$ are preferred contrary to the large eccentricity without the Keplerian prior. This is because Jacobian j_{kep} is proportional to $1/(e \sin i)$ as noted by Skowron et al. (2011) and thus smaller values of eccentricity are preferred. Here, technically, the lower limit of eccentricity is set to be 10^{-4} to avoid a numerical problem in MCMC as suggested by Skowron et al. (2011).

π_E is reduced by a factor of $1/2 \sim 2/3$ because the circular orbit is preferred by the Keplerian prior. So the lens masses increased, while the hosts are still the high-mass and low-mass brown dwarfs. As for the models $P_{\pm\mp}K_p$, there are other minima with a lower parallax value of $\pi_E \sim 0.2$ with similar final χ^2 whose host is a low-mass M-dwarf. This is because P_{kep} prefers larger values of D_l by D_l^6 . But χ^2 values from the light curves alone are larger than brown dwarf models. So there seems to be some conflict between light curve and prior.

4.4.3. *Stellar Kinematic constraint*

Here, we applied the prior for the Galactic kinematics by following Batista et al. (2011). In Table 11, the projected lens-source relative velocity $\tilde{\mathbf{v}}_t = (\tilde{v}_{t,l}, \tilde{v}_{t,b})$ of these K_p models in the Galactic coordinate differs significantly. Those of the M-dwarf models are significantly different from the expected value from the Galactic kinematics as shown in Fig. 8. Here we assume a source distance of $D_s = 8\text{kpc}$ (Reid 1993; Honma et al. 2012), the proper motion of the Galactic center is $\mu_{\text{GC}} = 6.1\text{ mas yr}^{-1}$ (Backer & Sramek 1999; Reid & Brunthaler 2004; Honma et al. 2012), the proper motion dispersion of stars in the bulge is $\sigma_{\mu, \text{GB}} = 3\text{ mas yr}^{-1}$ (Kuijken & Rich 2002), the velocity dispersions of the Galactic disk stars in the Galactic coordinates are $\sigma_{\text{Disk},l} = 34\text{ km s}^{-1}$ and $\sigma_{\text{Disk},b} = 18\text{ km s}^{-1}$ (Binney & Merrifield

1998; Minchev, Chiappini & Martig 2013; Sharma et al. 2014). Then the expected average $(\tilde{v}_{t,\text{exp},l}, \tilde{v}_{t,\text{exp},b})$ and dispersion $(\tilde{\sigma}_{t,l}, \tilde{\sigma}_{t,b})$ of the lens projected velocity are calculated. The probability of having observed $\tilde{\mathbf{v}}_t$ can be given by

$$P_{\text{kin}} = \exp \left[-\frac{(\tilde{v}_{t,l} - \tilde{v}_{t,\text{exp},l})^2}{2\tilde{\sigma}_{t,l}^2} \right] \exp \left[-\frac{(\tilde{v}_{t,b} - \tilde{v}_{t,\text{exp},b})^2}{2\tilde{\sigma}_{t,b}^2} \right]. \quad (4)$$

The $\Delta\chi^2$ penalty of $\Delta\chi_{\text{kin}}^2 = -2\ln(P_{\text{kin}})$ is about +16 and +15 for M-dwarf $P_{+-}K_p$ and $P_{-+}K_p$ models respectively. On the other hand the penalty is +9, +4, +2 and +2 for brown dwarf $P_{+-}K_p$, $P_{-+}K_p$, $P_{++}K_p$ and $P_{--}K_p$ models, respectively. So the M-dwarf models are less preferred.

Thus, we conducted MCMC runs by adding the penalty $\Delta\chi_{\text{kin}}^2$. The results (with scripts “ K_{pk} ”) are shown in Table 6, Table 12 and Figure 6. The model light curve of $P_{++}K_{\text{pk}}$ is shown in Figure 2. As expected, π_E values for the M-dwarf models increase to ~ 0.3 to reduce the $\Delta\chi_{\text{kin}}^2$ and the total χ^2 value became similar or larger than the brown dwarf models. In total, low-mass brown dwarf $P_{\pm\pm}K_{\text{pk}}$ models are slightly preferred over other models.

We adopt these K_{pk} models as our main results of this paper because they use the most realistic priors and constraints. See details in §4.5.

4.4.4. Galactic mass density prior

Finally, we applied the prior for the Galactic mass density model (Batista et al. 2011; Skowron et al. 2011).

$$P_{\text{gal}} = \nu(x, y, z)f(\mu)[g(M)M]\frac{D_l^4\mu^4}{\pi_E}, \quad (5)$$

which is the microlensing event rate multiplied by the Jacobian of the transformation from microlensing parameters to physical coordinates, $j_{\text{gal}} = ||\partial(D_l, M, \boldsymbol{\mu})/\partial(t_E, \theta_E, \boldsymbol{\pi}_E)||$. Here $\nu(x, y, z)$ is the local density of lenses, $g(M)$ is the mass function. $f(\mu)$ is the two-dimensional probability function for a given source-lens relative proper motion, $\mu = v_t/D_l$, which is set to unity because it is already implemented in P_{kin} above. We adopt the Galactic model by Han & Gould (1995) for $\nu(x, y, z)$ and adopt $g(M) \propto M^{-1}$ by following Batista et al. (2011).

The results of MCMC runs by adding a penalty of $\Delta\chi_{\text{gal}}^2 = -2\ln(P_{\text{gal}})$ are shown (with scripts “ K_{pkg} ”) in Table 7, Table 13 and Figure 6. The light curves, caustics, critical curves and source trajectory of the models comprising both parallax and planetary orbital motion with various different priors are almost same as that of the parallax-only models as shown

in Figure 2 and Figure 3. Overall, the lens masses slightly increased relative to that of K_{pk} models because this P_{gal} prefers larger D_l , i.e., smaller π_E .

In addition to above six models, there are two more minima for $P_{\pm\pm}K_{pkg}$ with a lower parallax value of $\pi_E \sim 0.8$ with similar final χ^2 values. This is also because the prior P_{gal} prefers larger D_l and smaller π_E values. These solutions happen to have similar π_E values with that of high-mass brown dwarf $P_{\pm\mp}K_{pkg}$ models, hence the similar physical parameters.

As for the $P_{\pm\mp}K_{pkg}$ models, there are two other minima which each have a much smaller parallax value of $\pi_E \sim 0.035$ and a smaller final $\chi^2 = 15107$. This is because their large values of $D_l = 7 \text{ kpc}$ are preferred by P_{gal} . These solutions have a very heavy host mass of $M_h \sim 1.7M_\odot$ which would be quite rare. In addition, these solutions have a value of $\chi^2_{lc} \sim 15224$ which is larger than any other model with parallax, which conflict to the preference by P_{gal} . Furthermore, these models have very bright H -band source magnitudes $H_s = 15.816 \pm 0.017$ and $H_s = 15.824 \pm 0.018$ for $P_{++}K_{pkg}$ and $P_{--}K_{pkg}$, respectively. These are too bright compared to the Keck AO measurement of the target, $H = 15.90 \pm 0.02$, by 3σ (see Section 6). If we assume that the host is a main sequence star, then total brightness of the source plus lens is expected to be brighter and ruled out by Keck measurements by more than 4σ . For these reasons we do not consider these solutions to be real, and are not listed amongst the other solutions in the Tables.

4.5. Model Selection

We have presented a large number of models with various high order effects and priors. Here we summarize which of these models are preferred over the others. As discussed in §4.2, the parallax signal looks qualitatively real because the signal come from the theoretically expected part of the light curve and it is consistent in both MOA and OGLE-*I* datasets. The χ^2 improvement by the parallax-only models over the standard model are $\Delta\chi^2 = -33.3 \sim -37.1$ with 2 additional parameters, which is equivalent to a confidence level of $5.4 \sim 5.8\sigma$ and is formally significant.

Furthermore, we compared the models by using the common statistical criteria, Akaike’s Information Criterion (AIC), $AIC = \chi^2 + 2n_{param}$, and the Bayesian information criterion (BIC), $BIC = \chi^2 + n_{param} \ln(N_{data})$ (Burnham & Anderson 2002), which includes a penalty discouraging an overfitting. The smaller the AIC and/or BIC values are the better model is. Here we adopt the number of data points $N_{data} = 2913$ during the event at $6450 < HJD' < 6620$ for BIC because the baseline data outside of this range do not constrain the parallax signal.

The differences in these criteria between the parallax-only models and standard model are $\Delta AIC = -29 \sim -33$ and $\Delta BIC = -17 \sim -21$. Thus the parallax-only models are better than the standard model. The parallax models with linear orbit (L) are also better than standard model by $\Delta AIC = -28 \sim -41$ and $\Delta BIC = -5 \sim -17$. The parallax models with full keplerian orbit with two more parameters are better than the standard in AIC but not in BIC .

The $\Delta\chi^2$ of the parallax models with linear orbit (L) relative to the parallax-only models are only marginal of $-3 \sim -12$ with two additional parameters. The differences in these criteria are $\Delta AIC = +0.7 \sim -8$ and $\Delta BIC = +13 \sim +4$, and it is worse for the full keplerian orbit with two more parameters. Thus, the inclusion of the orbital motion is not justified by these criteria.

However, the reason that we must introduce the orbital motion is not to improve the goodness of the fit, but to avoid the bias of the value and the underestimate of the uncertainty in parallax parameters due to the known degeneracy between the parallax and the lens orbital motion as shown in section §4.4.1.

Furthermore, even though the full Keplerian orbit does not improve the goodness of the fit with two additional parameters, its incorporation has the following benefits. As Skowron et al (2011) noted, in addition to being more accurate, the advantage of the full Keplerian orbit is to avoid all unbound orbital solutions (with eccentricity > 1) and to enable the introduction of priors on the values of orbital parameters directly into MCMC calculations. If the uncertainty of the parameters are relatively large like in this event, the density distribution of the MCMC chain depends on the prior probability of the fitting parameters in MCMC. However, the linear orbital motion parameterization inadvertently assumed the uniform prior on all microlensing fitting parameters, which is not physically justified. On the other hand, the full keplerian orbit parameterization enable us to properly weigh the MCMC chains with physically justified priors.

We conducted the modeling with three different sets of relatively realistic priors including the Keplerian prior, i.e., K_p , K_{pk} , and K_{pkg} . We think that the model K_{pk} is more realistic than K_p as the galactic kinematics constraint is applied. The models with the Galactic mass density prior K_{pkg} may also be useful, but we do not know if the assumption that the distribution of the planetary systems is uniform throughout the Galaxy is valid. Thus we adopt the K_{pk} models as our main results of this paper.

It is important to note that the results of all these models K_p , K_{pk} , and K_{pkg} , are basically same within their errors, thus our main conclusion does not depend on the choice of these priors.

Among the models in K_{pk} , the low-mass brown dwarf models, i.e., $P_{++}K_{\text{pk}}$ and $P_{--}K_{\text{pk}}$, are slightly preferred by both χ^2_{lc} , χ^2 and H_s (see §6). But we accept all the modes equally as possible solutions.

5. Lens properties

The lens physical parameters can be derived for this event because we could measure both the parallax and finite source effects in the light curve.

The OGLE-IV calibrated color magnitude diagram (CMD) in a $2' \times 2'$ region around the event is shown in Figure 9. Figure 9 also shows the center of the Red Clump giants (RCGs) $(V - I, I)_{\text{RC,obs}} = (2.047, 15.73) \pm (0.002, 0.04)$ and the model independent OGLE $V - I$ source color found by linear regression and the best fit source I magnitude of the model $P_{++}K_{\text{pk}}$, $(V - I, I)_s = (1.985, 18.13) \pm (0.008, 0.02)$. I_s for other models are almost same, as shown in Table 2-7.

Assuming the source suffers the same dust extinction and reddening as the RCGs and using the expected extinction-free RCG centroid $(V - I, I)_{\text{RC},0} = (1.06, 14.39) \pm (0.06, 0.04)$ at this position (Bensby et al. 2013; Nataf et al. 2013), we estimated the extinction-free color and magnitude of the source as $(V - I, I)_{s,0} = (1.00, 16.80) \pm (0.06, 0.06)$. This color measurement is consistent with the independent measurement of $(V - I)_{s,0} = 1.02 \pm 0.06$ by the CTIO telescope (see §3). We use the average of OGLE and CTIO colors, $(V - I)_{s,0} = 1.01 \pm 0.06$ in the following analyses. Here the errors in $(V - I)_{s,0}$ are dominated by the error in $(V - I)_{\text{RC},0}$. These values are consistent with the source being a K2 subgiant (Bessell & Brett 1988).

Following Fukui et al. (2015), we estimated the source angular radius, θ_* , by using the relation between the limb-darkened stellar angular diameter, θ_{LD} , $(V - I)$ and I given by Equation (4) of Fukui et al. (2015). This relation is derived from a subset of the interferometrically measured stellar radii in Boyajian et al. (2014), in which the dispersion of the relation is $\sim 2\%$ by using only stars with $3900\text{K} < T_{\text{eff}} < 7000\text{K}$ to improve the fit for FGK stars. This yield the source radius of $\theta_* = \theta_{\text{LD}}/2 = 1.84 \pm 0.12 \mu\text{as}$.

The spectrum of the source was taken by the UVES spectrograph on the Very Large Telescope (VLT) at a time when the source was still magnified as a Target of Opportunity (ToO) observation. Reductions were carried out with the UVES pipeline (Ballester et al. 2000). The observation and data analysis have been done by the same manor as Bensby et al. (2011, 2013). This gives the source effective temperature, $T_{\text{eff}} = 4854 \pm 66\text{K}$, the gravity, $\log g = 3.30 \pm 0.14$, and the metallicity, $[\text{Fe}/\text{H}] = -0.17 \pm 0.09$ (Bensby et al. in prepara-

tion). By using these values and the relation by Casagrande et al. (2010), we derive the extinction-free source colors, $(V - I)_{s,0,\text{spec}} = 1.036 \pm 0.047$ and $(V - H)_{s,0,\text{spec}} = 2.244 \pm 0.078$. Thus we get $(I - H)_{s,0,\text{spec}} = 1.208 \pm 0.091$. The extinction-free H -band source magnitude is given as $H_{s,0} = I_{s,0} - (I - H)_{s,0,\text{spec}} = 15.59 \pm 0.11$.

The expected extinction-free $(I - H)_{s,0}$ from the measured $(V - I)_{s,0}$ are $(I - H)_{s,0} = 1.188 \pm 0.082$ and $(I - H)_{s,0} = 1.119 \pm 0.074$ by using the stellar color-color relation of Bessell & Brett (1988) and Kenyon & Hartmann (1995), respectively. These are roughly consistent to $(I - H)_{s,0,\text{spec}}$. By a linear regression of OGLE- I -band light curve and CTIO H -band light curve (see §3), which are calibrated to the 2MASS scale, we got the source $(I - H)$ color as,

$$(I - H)_s = 2.256 \pm 0.016. \quad (6)$$

Correcting the extinction by using the measured extinction and reddening ($E(V - I)$, A_I) by RCGs and the extinction law of Chen et al. (2013), we got $(I - H)_{s,0,\text{OGLE,CTIO}} = 1.259 \pm 0.071$, which is also consistent with $(V - H)_{s,0,\text{spec}}$.

Then we got $\theta_* = 1.90 \pm 0.11 \mu\text{as}$ by using the relation between θ_{LD} , $H_{s,0}$, $(V - H)_{s,0}$ and $[\text{Fe}/\text{H}]$, given by Equation (9) of Fukui et al. (2015), which is also driven in the same way as Equation (4) of Fukui et al. (2015) but with the metallicity term. Note H in the relation is in Johnson magnitude system. Thus the observed H -band source magnitude which is in the 2MASS system, is converted to the Johnson system by following Fukui et al. (2015). This is consistent with above value. The average of above values are,

$$\theta_* = 1.87 \pm 0.12 \mu\text{as}, \quad (7)$$

where we adopt the larger error from the estimate with $(V - I, I)$, conservatively. This value is about the median of those from other models and differences from them are less than 2%, thus we adopt this value for all models in the following analysis.

We also tested the traditional method as follows. Following Yoo et al. (2004), the dereddened source color and brightness $(V - K, K)_{s,0} = (2.2, 15.6)$ are estimated using the observed $(V - I, I)_{s,0}$ and the color-color relation of Kenyon & Hartmann (1995). By using this $(V - K, K)_{s,0}$ relation and the empirical color/brightness-radius relation of Kervella et al. (2004), we estimated the source angular radius, $\theta_* = 1.85 \pm 0.16 \mu\text{as}$, where the error includes uncertainties in the color conversion and the color/brightness-radius relations. This is consistent with the above value.

The physical parameters of all models are listed in Table 8-13. The physical properties of three models with realistic priors and constraints, i.e., K_p , K_{pk} , and K_{pkg} , are basically same within the error bars. In the following analysis, we focus on the model K_{pk} .

Here we summarize the physical properties of the lens system by showing the average values of various models in Table 12 for clarity. The averages are taken without any weighting by their error bars. The uncertainties are given by the maximum and minimum values of 1- σ upper and lower limits of all (or a group of) models. The angular Einstein radii, and geocentric lens-source relative proper motion μ_{geo} , which are independent of the parallax values, are estimated, respectively, as follows,

$$\theta_E = \frac{\theta_*}{\rho} = 0.48 \pm 0.06 \text{ mas}, \quad (8)$$

$$\mu_{\text{geo}} = \frac{\theta_E}{t_E} = 8.4 \pm 1.2 \text{ mas yr}^{-1}. \quad (9)$$

This μ_{geo} is consistent with the typical value for disk lenses of $\mu \sim 5\text{--}10 \text{ mas yr}^{-1}$ (Han & Gould 1995).

The total mass and distance of the lens system can be given by $M = \theta_E/(\kappa\pi_E)$ and $D_1 = \text{AU}/(\pi_E\theta_E + \pi_s)$, where $\kappa = 4G/(c^2\text{AU})=8.144 \text{ mas } M_\odot^{-1}$, $\pi_s = \text{AU}/D_s$ and $D_s \sim 8 \text{ kpc}$ is the distance to the source (Dong et al. 2009b). Thus these quantities depend on the parallax parameter and we have three groups of solutions in models, i.e, small $\pi_E \sim 0.3$ ($P_{\pm\mp}K_{\text{pk}}$), medium $\pi_E \sim 0.8$ ($P_{\pm\mp}K_{\text{pk}}$ and $P_{\pm\pm}K_{\text{pk}}$) and large $\pi_E \sim 2$ ($P_{\pm\pm}K_{\text{pk}}$). The distance to the system, D_1 , the mass of the host, M_h , and planet, M_p , and their projected separation, a_\perp , of these solutions are,

$$D_1 = 3.6^{+0.6}_{-0.8} \text{ kpc}, 1.8^{+0.4}_{-0.2} \text{ kpc}, \text{ or } 0.85^{+0.13}_{-0.08} \text{ kpc}, \quad (10)$$

$$M_h = \frac{M}{1+q} = 0.19^{+0.05}_{-0.06} M_\odot, 0.068^{+0.019}_{-0.011} M_\odot, \text{ or } 0.025^{+0.005}_{-0.004} M_\odot, \quad (11)$$

$$M_p = \frac{qM}{1+q} = 21^{+6}_{-7} M_\oplus, 7.9^{+1.8}_{-1.2} M_\oplus, \text{ or } 3.2^{+0.5}_{-0.3} M_\oplus, \quad (12)$$

$$a_\perp = s\theta_E D_1 = 4.2^{+0.7}_{-0.9} \text{ AU}, 2.1^{+0.4}_{-0.2} \text{ AU}, \text{ or } 0.94^{+0.12}_{-0.09} \text{ AU}, \quad (13)$$

respectively. Here a_\perp is the 2-dimensional (2D) projection of a 3D elliptical orbit having a semi-major axis a . The expected 3D semi-major axis can be estimated by $a_{\text{exp}} = \sqrt{3/2}a_\perp$ (Gould et al. 2014). The best fit 3D semi-major axis by the Keplerian orbit, a_{kep} , are in-between of these values in the case of this event.

The semi-major axis a_{kep} normalized by the snow-line, $a_{\text{snow}} = 2.7(M_h/M_\odot)$, are

$$\frac{a_{\text{kep}}}{a_{\text{snow}}} = 8.9^{+10.5}_{-1.4}, \quad 12^{+7}_{-1}, \quad \text{or} \quad 14^{+11}_{-1}, \quad (14)$$

The effective temperature of the planet at the time of its formation based on the host mass and host-planet separation are also given in the tables.

The small parallax models suggest that the planet has a mass similar to Neptune ($17M_\oplus$) orbiting a very low mass M-dwarf in the Galactic disk. The planet is very cold as the estimated separation is $8.9^{+10.5}_{-1.4}$ times larger than the snow-line. This is comparable to Neptune’s semi-major axis, i.e., 11 times larger than the Sun’s snow-line. This interpretation of the planetary signal for MOA-2013-BLG-605Lb, therefore, suggests the planet is a Neptune analog.

The medium parallax models correspond to a miniature Neptune (or large-mass “super-Earth”) orbiting a high-mass brown dwarf host. The planet is even colder as the planetary orbit radius is 12^{+7}_{-2} times larger than the snow line, which is also similar to the Neptune.

The large parallax models correspond to three times the Earth-mass planet orbiting a low-mass brown dwarf host. The planet is colder because the planetary orbit radius is 14^{+11}_{-1} times larger than the snow line.

These solutions of K_{pk} are compared to the planets found by other methods in Figure 1. As one can see in the right-hand panel of Figure 1, in either group of models, this planet is the coldest low mass planet ever found and it is very similar to Neptune.

6. Keck AO Observations and Lens Mass constraint

We observed with the NIRC2 instrument mounted on KECK-II the microlensing target MOA-2013-BLG-0605 on July 26, 2015. We used the Wide camera giving a pixel scale of 0.04 arcsec and a field of view of 40 arcsec. We adopted a 5 position dithering pattern, and did 30 exposures of 10 seconds each. We performed dark subtraction and flatfielding in the standard manner for an IR detector. We then stacked the frames using Swarp (Bertin et al. 2002), without subtracting the background. The final image is shown in Figure 10.

For absolute calibration, we used images from the VVV survey done with the VISTA 4m telescope at Paranal (Minniti et al. 2010). We extracted a 3 arcmin JHK band images centred on the target. We computed a PSF model using PSFEX software (Bertin & Arnouts 1996), and measured fluxes on the frames using SExtractor with this PSF model. We cross identified the stars from the field with 2MASS catalogues. We selected 300 stars that are

bright while not saturated on VVV, and derive the photometric zero points with an accuracy of 0.004 mag. We then use the VVV catalogue to perform the astrometric calibration of the KECK frame.

We then measure the fluxes using SExtractor as described in (Batista et al. 2014). We cross identified 39 stars in both the VVV and KECK image. We exclude the stars saturated on the KECK, and derive the zero point of KECK photometry. In the non-AO PSF, there are two stars, the source with $H = 15.90 \pm 0.02$ and a blend at ~ 0.3 arcsec to the south with $H = 17.01 \pm 0.03$. Here, these two stars are blended in the OGLE reference image and the cataloged centroid is in-between of them. The actual source position during the magnification on the OGLE difference image was precisely measured as shown by the red cross in Figure 10. This clearly resolved the source and showed that the blend measured in the fitting process is not the lens.

By using the apparent source color $(I - H)_s$ given by Eq. (6) and the best fit I_s , H -band source magnitude, H_s are calculated as shown in Table 8-13. There is a trend that the smaller the parallax is, the brighter the source is. The H_s of low-mass brown dwarf models are almost same as the Keck measurement of $H = 15.90 \pm 0.02$ or only slightly brighter within 1σ . The H_s of high-mass brown dwarf and most of M-dwarf models are within 2σ . The M-dwarf models, $P_{-+}K_p$, $P_{-+}K_{pk}$ and $P_{-+}K_{pkg}$ have $H_s = 15.856 \pm 0.022$, 15.856 ± 0.024 , and 15.845 ± 0.026 , which are 1.6, 1.7 and 2.1 σ brighter than the Keck measurement. Furthermore, these are 2.0, 2.0 and 2.4 σ brighter when those include the lens (host) brightness (Kroupa & Tout 1997) of $H_h = 20.96 \pm 0.24$ ($M_h = 0.28M_\odot$, $D_l = 4.3\text{kpc}$), 21.22 ± 0.24 ($M_h = 0.20M_\odot$, $D_l = 3.5\text{kpc}$) and 21.17 ± 0.24 ($M_h = 0.21M_\odot$, $D_l = 3.7\text{kpc}$), respectively. These comparisons of the Keck result and source magnitudes from the light curve indicate that the lens is very faint and not detected. This is consistent with the physical solutions from the parallax measurements that the host is a low-mass M-dwarf or a brown dwarf mentioned in Section 5. The low-mass brown dwarf models are slightly preferred. The H_s of the standard model is consistent to the Keck results, but we concluded that the parallax models are better as discussed in §4.5.

As mentioned in Section 4.4.4, there are two minima with a much smaller parallax value of $\pi_E \sim 0.035$ for the $P_{\pm\mp}K_{pkg}$ models. In addition to the rarity of their heavy host mass of $\sim 1.7M_\odot$ which might be a stellar remnant, their source magnitudes $H_s = 15.824 \pm 0.018$ and $H_s = 15.816 \pm 0.017$ are 2.9σ and 3.2σ brighter than the Keck measurement. So these models are not likely real. If their host is a main sequence star, then total brightness of the source plus lens are ruled out by Keck measurement by more than 4σ .

7. Future Mass Measurement

Let us consider the prospects for resolving the degeneracy and characterizing the host and the planet. In the first epoch of Keck AO observations, we could not detect any excess light, which confirmed the lens is faint. If the second epoch is taken by *HST* or AO observations, then we may directly detect the host (or possibly its companion). We can then measure the lens mass and distance or place a stronger upper limit on the lens mass.

In Table 8-13, the geocentric proper motions are reported as $|\boldsymbol{\mu}_{\text{geo}}| = \theta_{\text{E}}/t_{\text{E}} = 8 \sim 9$ mas yr⁻¹. The heliocentric proper motion is given by (Janczak et al. 2010),

$$\boldsymbol{\mu}_{\text{hel}} = \boldsymbol{\mu}_{\text{geo}} + \mathbf{v}_{\oplus,\perp} \frac{\pi_{\text{rel}}}{\text{AU}}, \quad (15)$$

where $\mathbf{v}_{\oplus,\perp} = (v_{\oplus,\perp,N}, v_{\oplus,\perp,E}) = (-2.96, -8.24)$ km s⁻¹ is the velocity of the Earth projected on the plane of the sky at the peak of the event. The estimated $\boldsymbol{\mu}_{\text{hel}} = (\mu_{\text{hel},N}, \mu_{\text{hel},E})$ of each model is shown in Table 8-13, and they are about $8 \sim 9$ mas yr⁻¹. Hence it is clear that the lens will be separately resolved by *HST* or AO observations in 5-10 years' time given a diffraction limit of 50 mas. Or, if we do not see any luminous object, then the lens is a sub-stellar object.

Not only the value but also the direction of expected relative proper motion would help us to know if it was the lens or just an ambient star when we detect such star at 80mas from the source 10 years later.

8. Discussion and Conclusion

There are three physical planetary solutions for the MOA-2013-BLG-605L system. One comprises a Neptune-mass planet at a wide separation from a very low mass M-dwarf host star, having a very similar temperature as Neptune when the planet was formed. The second solution comprises a mini-Neptune around a high-mass brown dwarf which is even colder than Neptune when it was formed. The third one is a super-Earth around a low-mass brown dwarf.

These degenerate solutions may be resolved by future high resolution imaging of the lens by the *HST* or ground-based telescopes using adaptive optics, after waiting a period of time for the positions of the lens and the source to diverge. We may detect an M-dwarf lens host star, but we do not expect to detect a brown dwarf host star by such direct imaging.

In either case, the host is one of the three least massive main sequence stars orbited

by a planet for which the planet’s mass was measured and for which the planet-host mass ratio is $q < 0.01$. The other low host mass, low planet mass systems are MOA-2007-BLG-192L ($M_h = 0.084^{+0.015}_{-0.012} M_\odot$, $M_p = 3.2^{+5.2}_{-1.8} M_\oplus$, $r_\perp = 0.66^{+0.51}_{-0.22}$ AU) (Bennett et al. 2008; Kubas et al. 2012), MOA-2010-BLG-328L ($M_h = 0.11 \pm 0.01 M_\odot$, $M_p = 9.2 \pm 2.2 M_\oplus$, $r_\perp = 0.92 \pm 0.16$ AU) (Furusawa et al. 2013).

These planets found around very low mass ($\sim 0.1 M_\odot$) hosts have relatively small masses themselves, ranging from super-Earth mass to Neptune mass. In contrast, a roughly equal number of giant planets and planets with Neptune-mass or less have been found across the whole mass range of host stars. This may imply that the formation of gas giants is more difficult around very low mass stars compared to average K-M dwarf stars with masses of $\sim 0.5 M_\odot$, which is the typical host star for microlensing planets. This is somewhat as predicted by the core accretion model of planetary formation, but this work provides the first observational evidence supporting this prediction.

This could be the first exoplanet around a brown dwarf with a mass measurement having a planetary mass-ratio $q < 0.03$. There are three brown dwarf binaries where one of the components is in the planetary mass regime (Choi et al. 2013; Han et al. 2013). However, their mass ratios are large $q \geq 0.08$, suggesting that their formation may be considered more akin to binary formation than planetary formation.

The separation of the planet is very wide, $8.9^{+10.5}_{-1.4}$, 12^{+7}_{-1} or 14^{+11}_{-1} times larger than the snow line of $\sim 0.5(M/0.2 M_\odot)$ AU, $\sim 0.2(M/0.07 M_\odot)$ or $\sim 0.08(M/0.03 M_\odot)$ AU, respectively, as seen in Figure 1. The effective temperature of the planet when it was formed, based on the host mass and the planet-host separation, is ~ 26 K, ~ 13 K or ~ 7 K, the coldest planet found to date apart from those planets found by the direct imaging method, which can presently only find heavy gas-giant planets of more than a few Jupiter masses. The effective temperature of these heavy gas-giants are a few hundreds K or higher due to their internal heat. In either interpretation, planet MOA-2013-BLG-605Lb is orbiting around one of the least massive objects found to date at a very wide separation. The planet is the coldest exoplanet discovered so far. This is the first observed example of a Neptune-like exoplanet in terms of mass and temperature or a super-Earth with Neptune-like temperature, which are important factors in any planetary formation theory.

The probability of detecting such wide separation low mass planets is very low, even by microlensing. The probability of a source crossing the planetary caustic is proportional to the size of the planetary caustic, $w_c \sim 4q^{1/2}s^{-2} \sim 0.01$ (Han 2006), divided by half the circle with radius of separation s , i.e., $P \sim 4/\pi q^{1/2}s^{-3} \sim 1 \times 10^{-3}$ ($s = 2.4$). It is an order of magnitude smaller than planets at $s \sim 1$, where ~ 10 planets with Neptune-mass or less have been found by microlensing. This may imply that such low-mass planets with masses

less than that of Neptune at $a \simeq 10 a_{\text{snow}}$ are as common as low-mass planets at a few times of the snow line (Sumi et al. 2010; Gould et al. 2010; Cassan et al. 2012).

This conclusion may challenge the standard core accretion model and other formation models (Ida & Lin 2004) which predict few low-mass planets with Neptune-like orbit at $>10 a_{\text{snow}}$. More accurate measurements of the abundance and distribution of such low-mass ice planets are very important in the study of the formation of Neptune and in the study of planet formation mechanisms in general. The microlensing exoplanet search by NASA’s WFIRST satellite is expected to detect hundreds of low mass planets with Neptune-like orbit and will constrain further planetary formation models.

TS acknowledges the financial support from the JSPS, JSPS23103002, JSPS24253004 and JSPS26247023. The MOA project is supported by the grant JSPS25103508 and 23340064. The OGLE project has received funding from the National Science Centre, Poland, grant MAESTRO 2014/14/A/ST9/00121 to AU. DPB acknowledges support from NSF grants AST-1009621 and AST-1211875, as well as NASA grants NNX12AF54G and NNX13AF64G. Work by IAB and PY was supported by the Marsden Fund of the Royal Society of New Zealand, contract no. MAU1104. NJR is a Royal Society of New Zealand Rutherford Discovery Fellow. AS, ML and MD acknowledge support from the Royal Society of New Zealand. AS is a University of Auckland Doctoral Scholar. AG was supported by NSF grant AST 1103471 and NASA grant NNX12AB99G. J.P.B., S.B., J.B.M. gratefully acknowledges support from ESO’s DGDF 2014. JPB & JB acknowledge the support of the Programme National de Planétologie, CNRS, and from PERSU Sorbonne Université. Work by C.H. was supported by Creative Research Initiative Program (2009-0081561) of National Research Foundation of Korea.

REFERENCES

- Alard C., 2000, *A&AS*, 144, 363
- Alard C., Lupton R. H., 1998, *ApJ*, 503, 325
- Alcock, C., et al. 1995, *ApJ*, 454, 125
- Alcock, C., Alaskan, R. A., Alves, D. R., et al. 2001, *ApJ*, 552, 259
- An, J.H., Gould, A., 2001, *ApJ*, 563, L111
- Backer, D. C. & Sramek, R. A., 1999, *ApJ*, 524, 805

- Ballester, P., Modigliani, A., & Boitquin, O., et al. 2000, *The Messenger*, 101, 31
- Batista, V., et al. 2011, *ApJ*, 529, 102
- Batista, V., et al. 2014, *ApJ*, 780, 54
- Batista, V., Beaulieu, J.-P., Bennett, D.P. et al. 2015, *ApJ*, submitted
- Bessell, M. S., & Brett, J. M. 1988, *PASP*, 100, 1134
- Bennett, D.P. & Rhie, S.H. 1996, *ApJ*, 472, 660
- Bennett, D. P., Anderson, J., Bond, I. A., Udalski, & A., Gould, A. 2006, *ApJ*, 647, 171
- Bennett, D. P., Bhattacharya, A., Anderson, J., et al. 2015, *ApJ*, submitted
- Bennett, D. P., Bond, I. A., Udalski, A., et al. 2008, *ApJ*, 684, 663
- Bennett, D. P., Rhie, S. H., Nikolaev, S., et al. 2010, *ApJ*, 713, 837
- Binney, J., & Merrifield, M. 1998, *Galactic Astronomy* (Princeton, NJ:Princeton Univ. Press)
- Bensby, T., et al. 2011, *A&A*, 533, A134
- Bensby, T., Yee, J. C., Feltzing, S., et al. 2013, *A&A*, 549, A147
- Berta, Z. K. ; Irwin, J., Charbonneau, D., 2013, *ApJ*, 775, 91
- Bertin, E., & Arnouts, S. 1996, *A&AS*, 117, 393
- Bertin, E., Mellier, Y., Radovich, M., Missonnier, G., Didelon, P., & Morin, B. 2002, in
ASP Conf. Ser. 281, *Astronomical Data Analysis Software and Systems XI*, ed. D. A.
Bohlender, D. Durand, & T. H. Handley (San Francisco, CA: ASP), 228
- Bond I. A. et al., 2001, *MNRAS*, 327, 868
- Borucki, W. J., Koch, D. G., Batalha, N., et a. 2012, *ApJ*, 745, 120
- Boyajian, T. S., van Belle, G., & von Braun, K. 2014, *AJ*, 147, 47
- Burke, Christopher J. et a. 2014, *ApJS*, 210, 19
- Burnham, K. P. & Anderson, D. R. 2002, *Model Selection and Multimodel Inference* (2nd ed.), Springer

- Casagrande, L., Ramírez, I., Meléndez, J., Bessell, M., & Asplund, M. , 2010, *A&A*, 512, A54
- Cassan, A., Kubas, D., Beaulieu, J.-P., et al. 2012, *Nature*, 481, 167
- Clanton, C. & Gaudi, B.S., 2014, *ApJ*, 791, 91
- Claret, A. 2000, *A&A*, 363, 1081
- Chen, B. Q., Schultheis, M., Jiang, B. W., et al. 2013, *A&A*, 550, A42
- Choi, J.-Y., Han, C., Udalski, A., et al. 2013, *ApJ*, 768, 129
- Derue, F., Afonso, C., et al. 1999, *A&A*, 351, 87
- Dong, S., Gould, A., Udalski, A., et al. 2009a, *ApJ*, 695, 970
- Dong, S., Bond, I. A., Gould, A., et al. 2009b, *ApJ*, 698, 1826
- Dressing, C. D. & Charbonneau, D, 2013, *ApJ*, 767, 95
- Fernandez, J. A.; Ip, W.-H. 1984, *Icarus*, 58, 109
- Fukui, A. et al. 2015, *ApJ*, 809, 74
- Furusawa, K. et al. 2013, *ApJ*, 779, 91
- Gaudi, B. S., Bennett, D. P., Udalski, A., et al. 2008, *Science*, 319, 927
- Gould, A. 1992, *ApJ*, 392, 442
- Gould, A. 1994, *ApJ*, 421, L75
- Gould, A. et al. 2009, *ApJ*, 698, L147
- Gould, A., et al. 2010, *ApJ*, 720, 1073
- Gould, A., et al. 2014, *Science*, 345, 46
- Gould, A. 2004, *ApJ*, 606, 319
- Griest, K., & Hu, W. 1992, *ApJ*, 397, 362
- Han, C. & Gould, A. 1995, *ApJ*, 449, 521
- Han, C., 2006, *ApJ*, 638, 1080

- Han, C., & Gould, A. 1997, *ApJ*, 480, 196
- Han, C. & Gould, A. 2003, *ApJ*, 592, 172
- Han, C., Jung, Y. K., Udalski, A., et al. 2013, *ApJ*, 778, 38
- Helled, R. & Bodenheimer, P. 2014, *ApJ*, 789, 69
- Honma, M., et al. 2012, *PASJ*, 64, 136
- Ida, S., & Lin, D.N.C. 2004, *ApJ*, 616, 567
- Janczak, J. et al. 2010, *ApJ*, 711, 731
- Kains N. et al. 2013, *A&A*, 552, 70
- Kennedy, G. M., Kenyon, S. J., & Bromley, B. C. 2006, *ApJ*, 650, L139
- Kennedy, G. M., Kenyon, S. J., 2008, *ApJ*, 673, 502
- Kenyon, S. J. & Hartmann, L., 1995, *ApJS*, 101, 117
- Kervella, P., & Fouqué, P. 2008, *A&A*, 491, 855
- Kervella, P., Thévenin, F., Di Folco, E., & Ségransan, D. 2004, *A&A*, 426, 297
- Kroupa, P. & Tout, C. A., 1997, *MNRAS*, 287, 402
- Kubas, D., Beaulieu, J. P., Bennett, D. P., et al. 2012, *A&A*, 540, 78
- Kuijken, K. & Rich, R. M. 2002, *AJ*, 124, 2054
- Laughlin, G., Bodenheimer, P., & Adams, F.C. 2004, *ApJ*, 612, L73
- Malhotra, R., 1993, *Nature*, 365, 819
- Mayor, M., & Queloz, D. 1995, *Nature*, 378, 355
- Minchev, I., Chiappini, C. & Martig, M 2013, *A&A*, 558, A9
- Minniti, D., Lucas, P. W., Emerson, J. P., et al. 2010, *New A*, 15, 433
- Montet, B. T., Crepp, J. R., Johnson, J. A., Howard, A. W., Marcy, G. W., 2014, *ApJ*, 781, 28
- Morton, T. D. & Swift, J. J., 2014, *ApJ*, 791, 10

- Muraki, Y., et al. 2011, ApJ, 741, 22
- Nataf, D. M. et al. 2013, ApJ, 769, 88
- Calchi Novati S., et al. 2015a, ApJ, 804, 20
- Calchi Novati S., et al. 2015b, ApJ, 814, 92
- Park, B. -G. et al. 2004, ApJ, 609, 166
- Refsdal, S. 1966, MNRAS, 134, 315
- Reid, M. J. 1993, ARA&A, 31, 345
- Reid, M. J. & Brunthaler, A., 2004, ApJ, 616, 872
- Poleski, R. et al., 2014, ApJ, 795, 42
- Pollack, J. B., Hubickyj, O., Bodenheimer, P., et al. 1996, Icarus, 124, 62
- Quintana, E.V., Barclay, T., Raymond, S.N. et al. 2014, Science, 344, 277
- Sharma, S., et al. 2014, ApJ, 793, 51
- Schechter, L., Mateo, M., & Saha, A., 1993, PASP, 105, 1342S
- Skowron, J., Udalski, A., Gould, A., et al. 2011, ApJ, 738, 87
- Smith, M. C., Mao, S., & Paczyński, B. 2003, MNRAS, 339, 925
- Smith, M. C., Mao, S. & Woźniak, P. R., 2002, MNRAS, 332, 962
- Sumi, T. et al., 2003, ApJ, 591, 204
- Sumi, T. et al., 2010, ApJ, 710, 1641
- Sumi, T. et al., 2011, Nature, 473, 349
- Tsapras T. et al. 2014, ApJ, 782, 48
- Tomany, A. B. & Crotts, A. P., 1996, AJ, 112, 2872
- Thommes, E. W., Duncan, M. J. & Levison, H. F., 1999, Natur, 402, 635
- Udalski, A. 2003, Acta Astron., 53, 291
- Udalski,A., Szymański, M.K. and Szymański, G. 2015, Acta Astronomica, 65, 1

- Udalski A. et al. 2015, ApJ, 799, 237
- Verde L., et al, 2003 ApJS, 148,195
- Wittenmyer, R. A., et al. 2014, ApJ, 783, 103
- Woźniak P. R., 2000, Acta Astronomica, 50, 421
- Yee, J. C., Shvartzvald, Y., Gal-Yam, A., et al. 2012, ApJ, 755, 102
- Yoo, J., et al, 2004a ApJ, 603, 139

Table 1. Datasets used in the analysis

Dataset	Telescope	Filter	N_{data}	k	e_{min}
MOA-Red	MOA-II 1.8 m	$R + I$	9675	1.092	0.0127
OGLE-I	Warsaw 1.3 m	I	5514	1.387	0.0109
OGLE-V	Warsaw 1.3 m	V	64	1.571	0.0
CTIO-I	SMARTS-CTIO 1.3 m	I	15	1.0	0.0
CTIO-V	SMARTS-CTIO 1.3 m	V	15	1.0	0.0
CTIO-H	SMARTS-CTIO 1.3 m	H	149	1.0	0.0

Note. — N_{data} is the number of data points used in the analysis. k and e_{min} are the error scaling parameters (see details in the text).

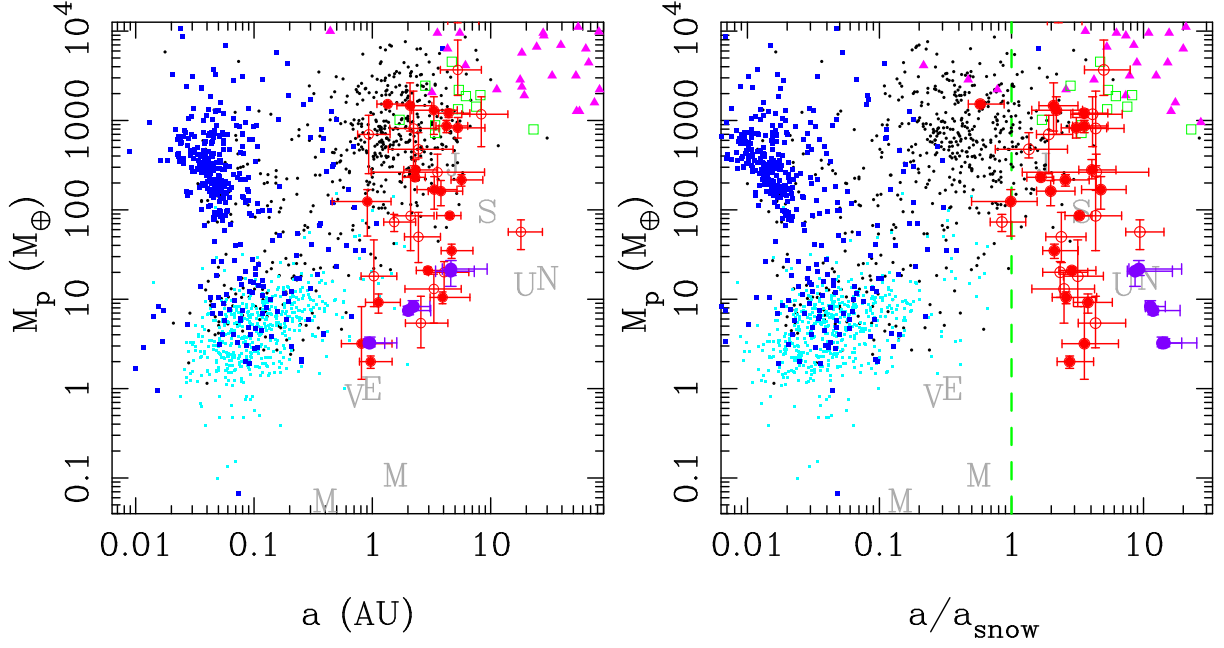


Fig. 1.—: The distribution in planetary mass, M_p , versus the semi-major axis, a (left panel) and a normalized by the snow-line (right panel) of discovered exoplanets by various methods. Red circles indicate the microlensing planets. Microlensing planets for which mass measurements have been made are indicated with filled circles. Microlensing planets where the mass has been estimated by a Bayesian analysis are indicated with open circles. The six model solutions for event MOA-2013-BLG-605Lb comprising parallax and the Keplerian orbital motion with the Keplerian prior and the kinematic constraint (K_{pk}) are indicated by purple filled circles. Black dots represent the radial velocity planets and blue filled squares are transit planets. Cyan dots are transit planets found by *Kepler*. Magenta triangles denote planets found via direct imaging. Green open squares denotes planets found via timing measurements. Solar system planets are indicated by their initial. A green vertical dashed line indicates the snow line. All models for MOA-2013-BLG-605Lb are very similar to Neptune, when planet orbit radii are scaled to the snow line (right panel).

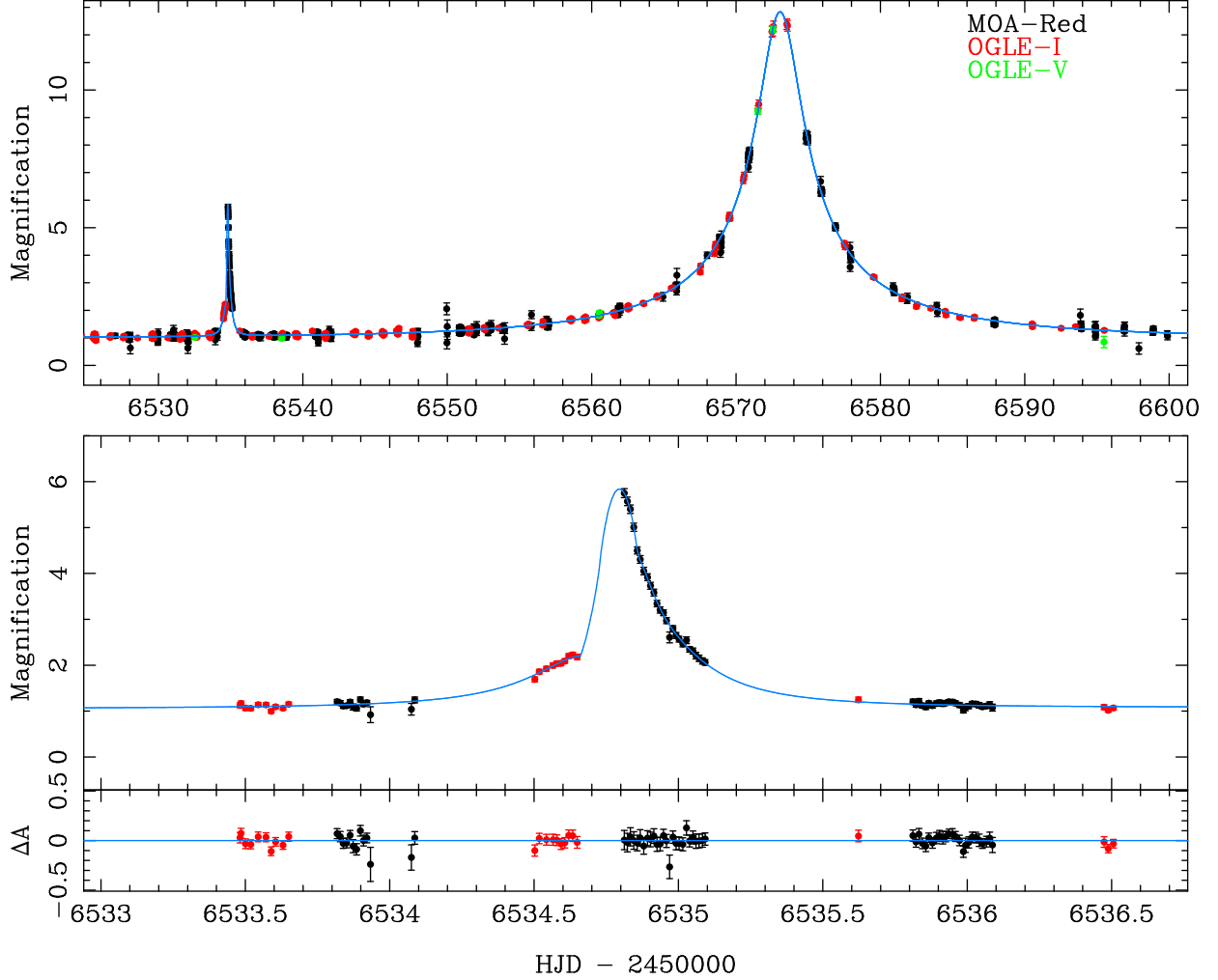


Fig. 2.—: Light curve of MOA-2013-BLG-605. Black, red and green points indicate MOA-Red, OGLE-I and OGLE-V band data, respectively. Blue lines represent the parallax model with Keplerian orbital motion, a Keplerian prior and the kinematic constraint $P_{++}K_{pk}$ which is almost identical to all models with parallax and orbital motion. Middle and Bottom panels show the detail of the planetary signal and its residual from the best model.

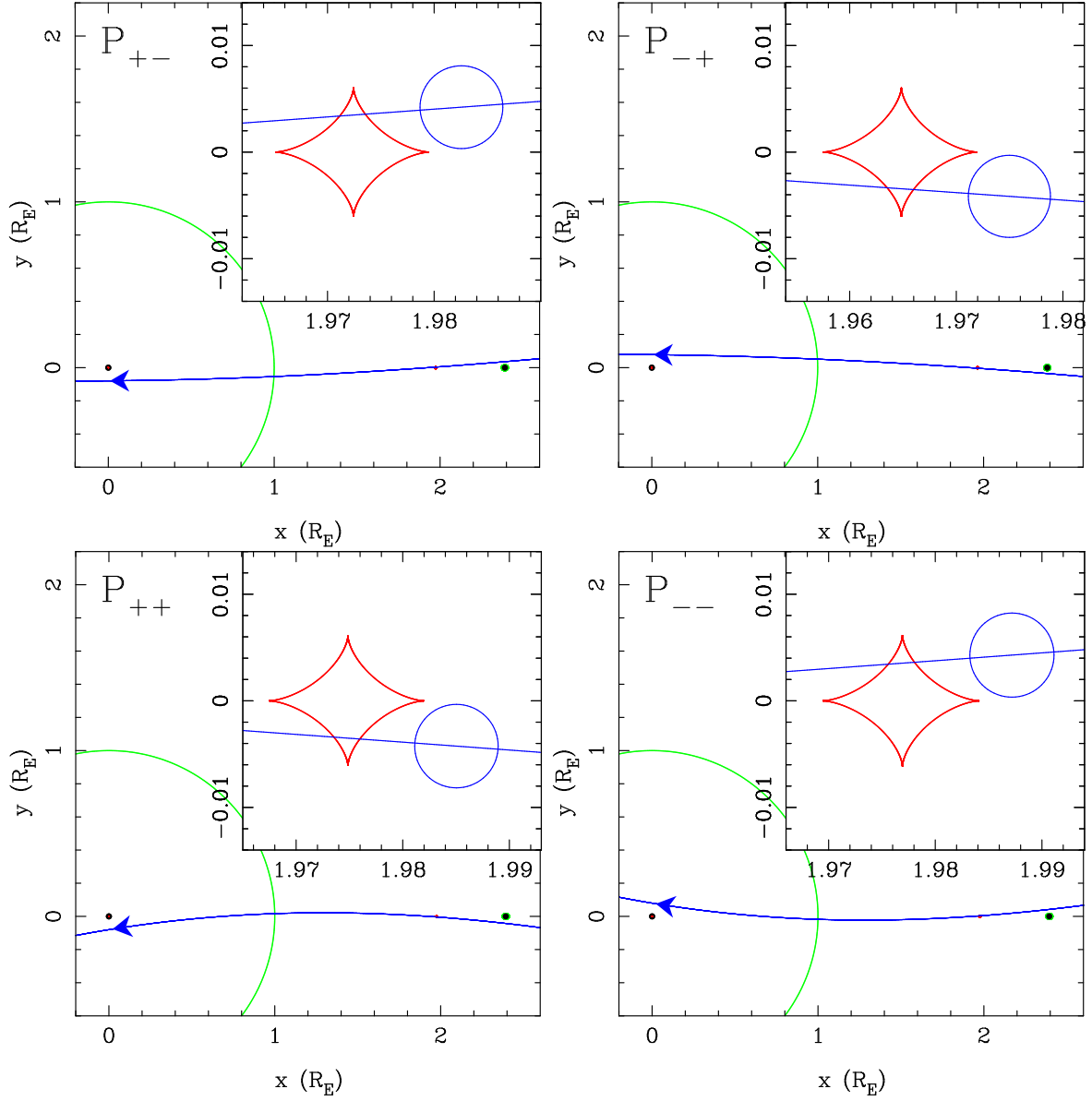


Fig. 3.— Caustics (Red lines) of MOA-2013-BLG-605 of the best fit parallax models, P_{+-} , P_{-+} , P_{++} and P_{--} in top-left, top-right, bottom-left and bottom-right panel, respectively. The figure of each model with a orbital motion and various priors are similar. Insets show a close-up view around the planetary caustic. Blue circles indicate the best fit source star radius and position at HJD= 6534.6, just before crossing the planetary caustic. Blue lines with arrows represent source star trajectories. The left and right black filled circles at $y = 0$ indicate the positions of primary and planet, respectively. The green lines show critical curves.

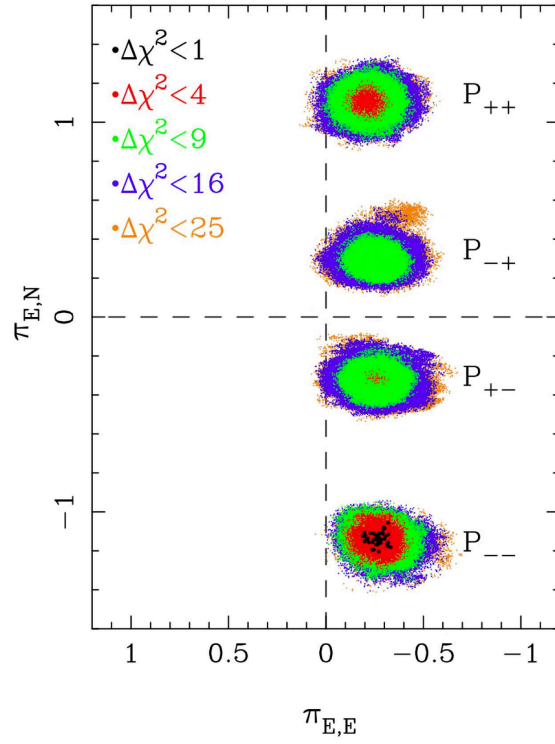


Fig. 4.—: $\Delta\chi^2$ distribution of the parallax parameters from the best fit parallax-only models, without orbital motion, P_{++} , P_{-+} , P_{+-} and P_{--} , from top to bottom. Black, red, green, blue and orange dots indicate chains with $\Delta\chi^2 < 1, 4, 9, 16$ and 25 , respectively. The black dots are larger than the others for clarity.

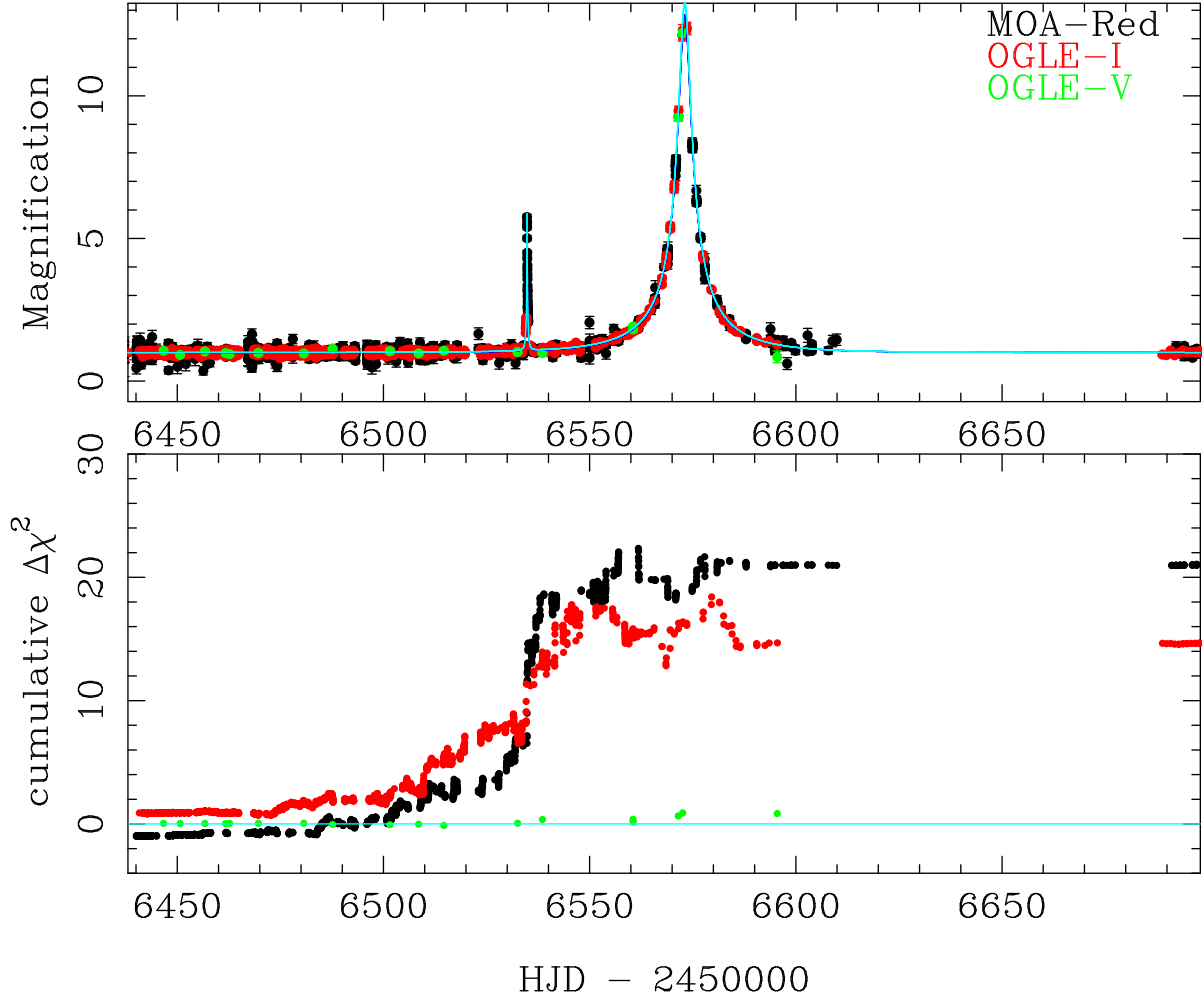


Fig. 5.—: The difference in the cumulative χ^2 values between the standard and the parallax models, $\chi^2_{\text{standard}} - \chi^2_{\text{parallax}}$, is shown as a function of time in the bottom panel. This is the case of the parallax model with an orbital motion, keplerian prior and kinematic prior, P₊₊K_{pk} (see section §4.4.3), but it is similar for all models with parallax. The corresponding light curve is given in the top panel as a reference. Blue and cyan solid lines represent the standard and P₊₊K_{pk} models, while the cyan line almost overlaps the blue one. Black, red and green points represent MOA-Red, OGLE-I and OGLE-V, respectively. The plots are slightly shifted to match at the beginning of 2013 season for clarity, where the total $\Delta\chi^2$ in the baseline outside of the figure is almost zero. We can see that most of the parallax signals come from around the planetary signal in both MOA-Red and OGLE-I as expected. This consistency in two datasets support the reality of the parallax signal.

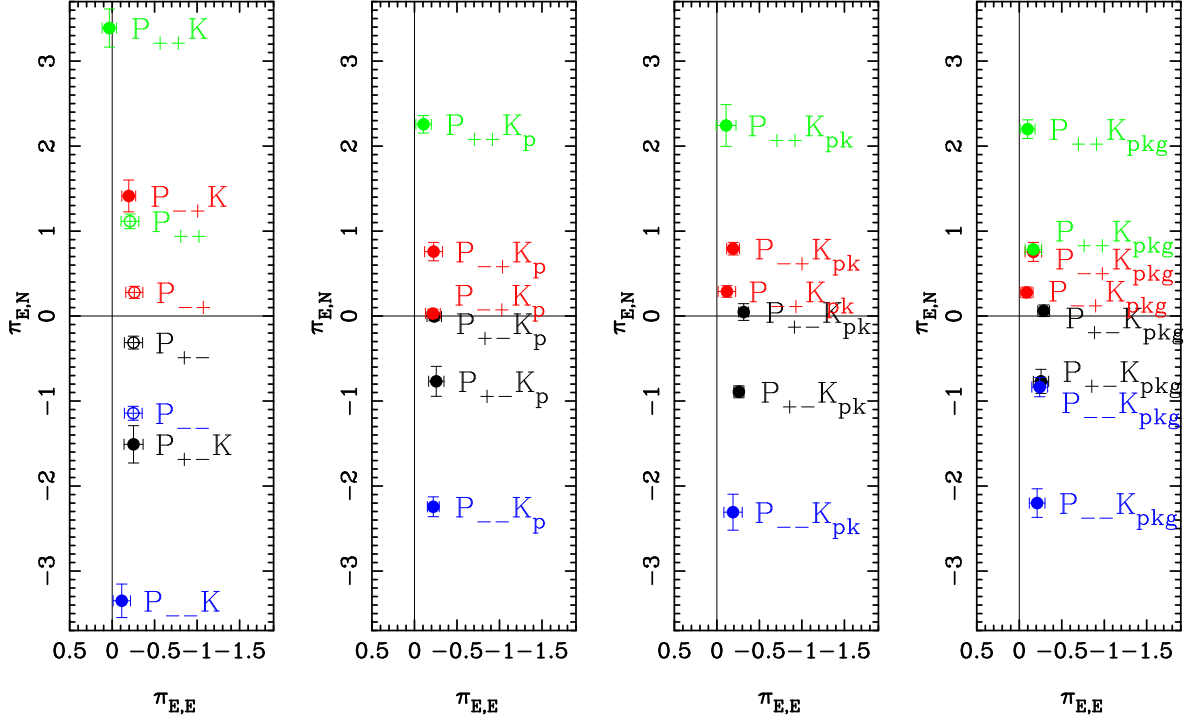


Fig. 6.—: The best fit parallax parameters ($\pi_{E,E}$, $\pi_{E,N}$) of the parallax-only model (open circles in the left panel) and the parallax with the orbital motion (filled circles) with the Keplerian orbit (K), the Keplerian prior (K_p), kinematic constraint (K_{pk}) and the Galactic prior (K_{pkg}) from the left to right panels, respectively. The black, red, green and blue color-code correspond the models with the geometry of P_{+-} , P_{-+} , P_{++} and P_{--} , respectively. The linear orbital motion models (L) are omitted for clarity, because they are almost same as the Keplerian orbit models (K).

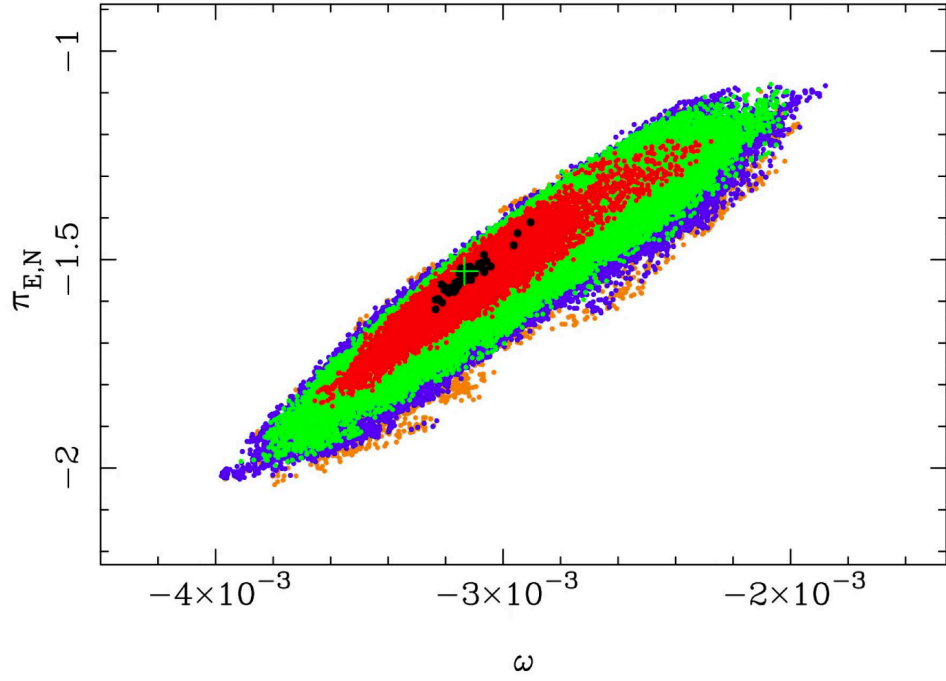


Fig. 7.—: $\Delta\chi^2$ distribution of the parallax parameter $\pi_{E,N}$ and orbital motion perimeter ω from the best fit MCMC models of the P₊₋L, the parallax with a linear orbital motion model. Black, red, green, blue and orange dots indicate chains with $\Delta\chi^2 < 1, 4, 9, 16$ and 25 , respectively. Here ω is in rad day^{-1} as actually used in the MCMC. The black dots are larger than the others for clarity.

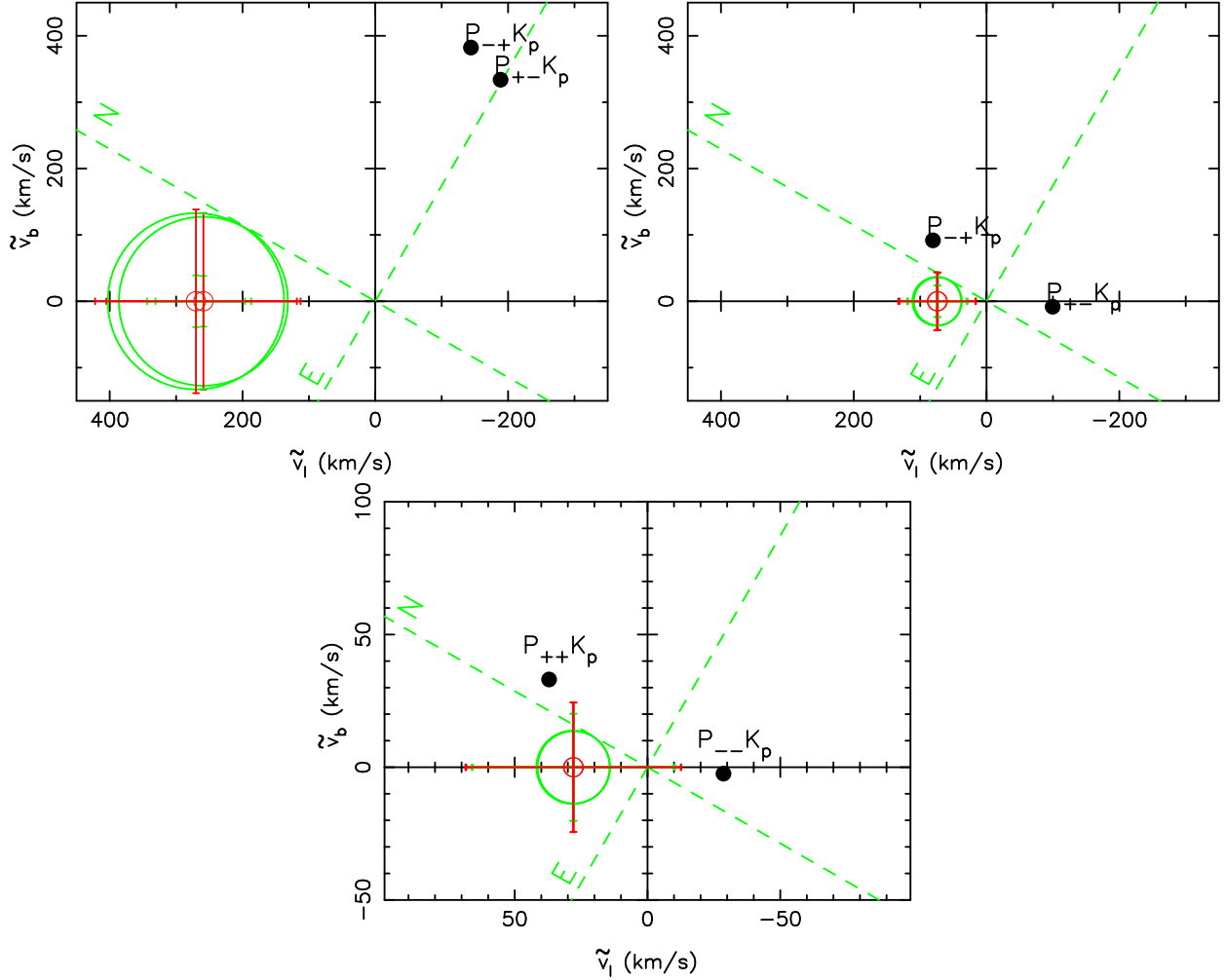


Fig. 8.—: Lens projected velocity $\tilde{\mathbf{v}}_t = (\tilde{v}_l, \tilde{v}_b)$ in the Galactic coordinate from the best fit with Keplerian orbit with the Keplerian prior. Top-left, top-right and bottom panels indicate M-dwarf and brown dwarf $P_{\pm\mp}K_p$ models and brown dwarf $P_{\pm\pm}K_p$ models, respectively. Red circles are expected mean from the Galactic kinematics. Green error bars and circles represent uncertainty due to the velocity dispersion of disk stars and bulge stars, respectively. They are added in the quadrature in the total error shown in red error bars. Green dashed line indicate the ecliptic North and East. The $\tilde{\mathbf{v}}_t$ of M-dwarf $P_{\pm\mp}K_p$ models are significantly different from the expected value from the Galactic kinematics.

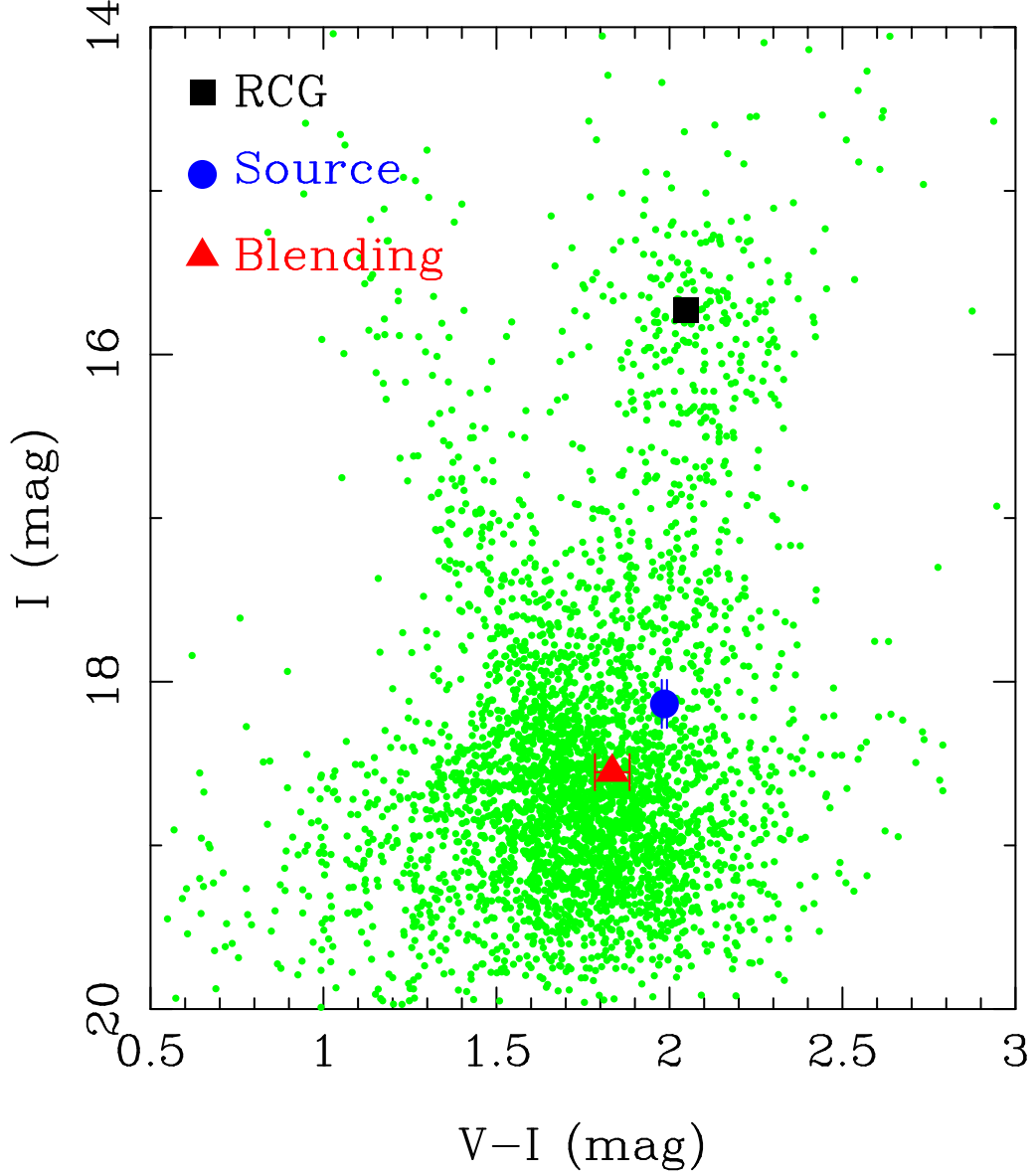


Fig. 9.—: OGLE-IV calibrated V and I Color magnitude diagram (CMD) within $2' \times 2'$ around the event (green dots). A filled square indicates the center of Red Clump Giants. The source position of $P_{++}K_{pk}$ model shown by the filled circle, which is almost identical for all models, indicates that the source star is a K2 sub-giant.

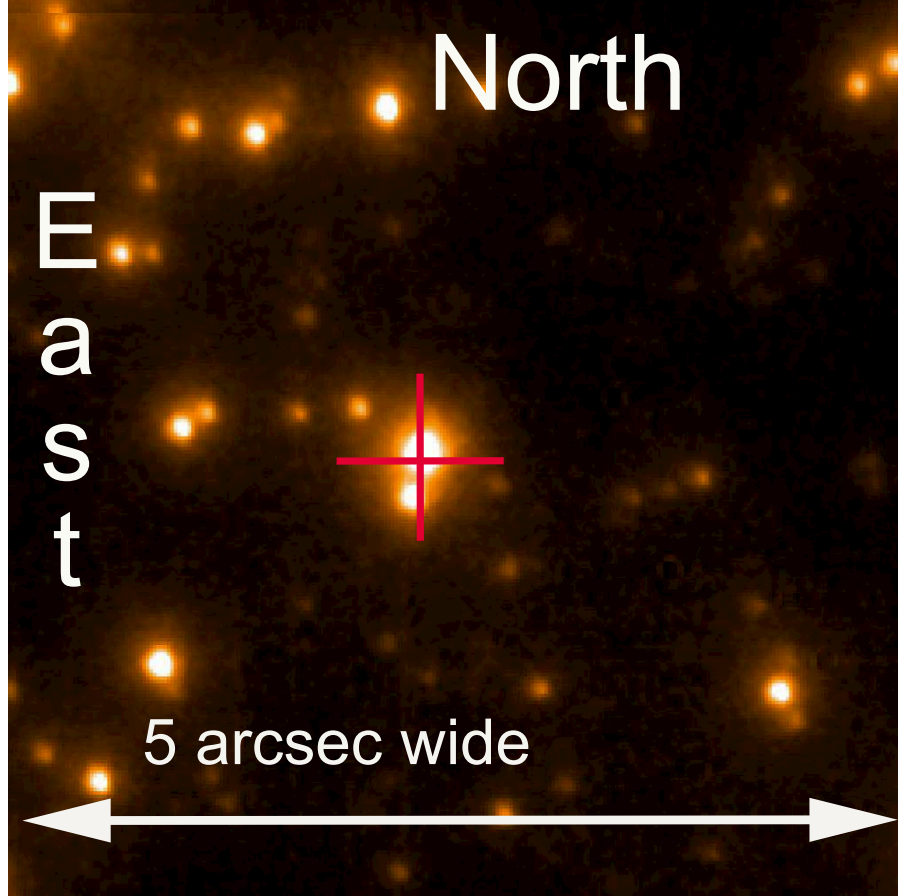


Fig. 10.—: H -band Keck AO image within $5'' \times 5''$ around the event. The red cross indicates the actual source position measured during the magnification on the OGLE difference image. The brighter star at the cross is the source with $H = 15.90 \pm 0.02$ mag. The fainter star on South is the blend with $H = 17.01 \pm 0.02$ mag. This shows that the blend measured in the fitting process is not the lens. The measured H -band flux of the source shows that the lens is very faint and not detected.

Table 2. Model Parameters. Standard and Parallax-only models.

Parameter	Standard	P ₊₋	P ₋₊	P ₊₊	P ₋₋
t_0 (HJD')	6573.056	6573.050	6573.050	6573.051	6573.052
	0.008	0.009	0.009	0.009	0.010
t_E (days)	20.47	19.93	20.04	20.10	20.15
	0.13	0.32	0.29	0.32	0.28
u_0 (10^{-2})	7.563	7.932	-7.874	7.907	-7.890
	0.099	0.186	0.175	0.185	0.164
q (10^{-4})	2.762	3.460	3.431	3.530	3.611
	0.105	0.211	0.204	0.202	0.215
s	2.304	2.391	2.384	2.393	2.395
	0.010	0.019	0.018	0.020	0.017
α_0 (radian)	3.0996	3.1335	3.1534	2.9829	3.3035
	0.0004	0.0077	0.0072	0.0084	0.0080
ρ (10^{-3})	3.37	3.88	3.85	3.91	3.95
	0.10	0.15	0.14	0.15	0.14
$\pi_{E,N}$	0.000	-0.313	0.279	1.114	-1.144
	0.000	0.076	0.071	0.086	0.082
$\pi_{E,E}$	0.000	-0.252	-0.261	-0.210	-0.249
	0.000	0.107	0.100	0.104	0.104
π_E	0.000	0.401	0.382	1.134	1.170
	0.000	0.088	0.082	0.084	0.088
I_s (mag)	18.167	18.117	18.125	18.120	18.123
	0.011	0.024	0.023	0.025	0.021
I_b (mag)	18.508	18.580	18.568	18.575	18.571
	0.015	0.037	0.034	0.038	0.032
H_s (mag)	15.911	15.861	15.869	15.864	15.867
	0.019	0.029	0.028	0.029	0.027
χ^2_{lc}	15251.42	15217.49	15218.15	15216.43	15214.27
$\Delta\chi^2_{kep}$	0.00	0.00	0.00	0.00	0.00
$\Delta\chi^2_{kin}$	0.00	0.00	0.00	0.00	0.00
$\Delta\chi^2_{gal}$	0.00	0.00	0.00	0.00	0.00
χ^2	15251.42	15217.49	15218.15	15216.43	15214.27
dof	15217	15215	15215	15215	15215

Note. — HJD' = HJD - 2450000. The first subscript of model P, “+” and “-” indicate the models with $u_0 > 0$ and $u_0 < 0$, respectively. The second subscript indicates the sign of impact parameter to the secondary lens, i.e., “++” and “--” mean the source passes on the same side to the host and planet. The 1σ error is given below each parameter. χ^2_{lc} is the χ^2 from the light curve alone. $\Delta\chi^2_{kep}$, $\Delta\chi^2_{kin}$ and $\Delta\chi^2_{gal}$ are χ^2 penalty due to the Keplerian, kinematic and the Galactic priors. Note that π_E is not a fit parameter.

Table 3. Model Parameters. Linear orbit (L).

Parameter	P ₊₋ L	P ₋₊ L	P ₊₊ L	P ₋₋ L	P ₊₊ L'	P ₋₋ L'
t_0 (HJD')	6573.051	6573.051	6573.055	6573.055	6573.055	6573.055
	0.006	0.009	0.010	0.010	0.010	0.010
t_E (days)	19.95	19.90	21.33	21.24	21.25	21.22
	0.32	0.22	0.31	0.33	0.35	0.34
u_0 (10^{-2})	7.869	-7.894	7.418	-7.452	7.455	-7.449
	0.187	0.128	0.154	0.169	0.169	0.161
q (10^{-4})	3.614	3.422	4.183	4.913	2.805	2.846
	0.201	0.260	0.355	0.474	0.491	0.220
s_0	2.370	2.353	2.302	2.451	1.972	1.975
	0.024	0.063	0.093	0.081	0.111	0.022
α_0 (radian)	3.1445	3.1444	2.9485	3.3412	2.9614	3.3222
	0.0067	0.0076	0.0058	0.0144	0.0097	0.0126
ρ (10^{-3})	3.94	3.85	4.06	4.41	3.33	3.36
	0.12	0.19	0.19	0.23	0.28	0.12
$\pi_{E,N}$	-1.528	1.420	3.731	-3.366	3.703	-3.326
	0.194	0.226	0.213	0.340	0.283	0.318
$\pi_{E,E}$	-0.240	-0.191	0.070	-0.138	0.077	-0.143
	0.106	0.074	0.092	0.114	0.112	0.111
π_E	1.546	1.433	3.732	3.369	3.704	3.330
	0.194	0.225	0.213	0.337	0.284	0.317
ω (rad yr $^{-1}$)	-1.145	1.087	2.459	-1.974	2.550	-2.117
	0.132	0.185	0.210	0.214	0.269	0.227
ds/dt (yr $^{-1}$)	-0.277	-0.403	-0.935	0.434	-4.104	-4.099
	0.376	0.588	0.921	0.829	1.049	0.244
s_z	0.000	0.000	0.000	0.000	0.000	0.000
	0.000	0.000	0.000	0.000	0.000	0.000
ds_z/dt (yr $^{-1}$)	0.000	0.000	0.000	0.000	0.000	0.000
	0.000	0.000	0.000	0.000	0.000	0.000
I_s (mag)	18.126	18.122	18.190	18.186	18.185	18.185
	0.025	0.017	0.021	0.023	0.024	0.023
I_b (mag)	18.566	18.572	18.476	18.481	18.482	18.482
	0.037	0.026	0.028	0.031	0.031	0.030
H_s (mag)	15.870	15.866	15.934	15.930	15.929	15.929
	0.029	0.024	0.027	0.028	0.029	0.028
χ^2_{lc}	15212.02	15214.89	15204.17	15204.36	15202.31	15202.52
$\Delta\chi^2_{kep}$	0.00	0.00	0.00	0.00	0.00	0.00
$\Delta\chi^2_{kin}$	0.00	0.00	0.00	0.00	0.00	0.00
$\Delta\chi^2_{gal}$	0.00	0.00	0.00	0.00	0.00	0.00
χ^2	15212.02	15214.89	15204.17	15204.36	15202.31	15202.52
dof	15213	15213	15213	15213	15213	15213

Note. — Notation is ame as Table 2. The solutions P_{±±}L' does not exist with the full Keplerian orbit.

Table 4. Model Parameters. Full keplerian orbit (K).

Parameter	P _{+-K}	P _{-+K}	P _{++K}	P _{--K}
t_0 (HJD')	6573.051	6573.051	6573.054	6573.055
	0.010	0.008	0.009	0.008
t_E (days)	19.98	19.91	21.03	21.14
	0.22	0.27	0.22	0.18
u_0 (10^{-2})	7.856	-7.886	7.553	-7.488
	0.134	0.157	0.119	0.085
q (10^{-4})	3.789	3.663	4.216	5.197
	0.196	0.211	0.335	0.317
s_0	2.423	2.418	2.396	2.535
	0.018	0.026	0.055	0.033
α_0 (radian)	3.1474	3.1410	2.9553	3.3528
	0.0077	0.0075	0.0122	0.0080
ρ (10^{-3})	4.03	3.98	4.12	4.56
	0.11	0.13	0.17	0.19
$\pi_{E,N}$	-1.509	1.413	3.389	-3.351
	0.220	0.187	0.224	0.197
$\pi_{E,E}$	-0.252	-0.196	0.033	-0.114
	0.112	0.081	0.084	0.103
π_E	1.530	1.427	3.389	3.353
	0.219	0.181	0.225	0.194
ω (rad yr $^{-1}$)	-1.086	1.036	2.140	-1.744
	0.179	0.130	0.155	0.156
ds/dt	0.304	0.293	0.241	1.431
(yr $^{-1}$)	0.240	0.203	0.577	0.356
s_z	0.002	0.031	0.025	0.602
	0.122	0.200	0.078	0.288
ds_z/dt	0.108	0.005	-0.413	-0.695
(yr $^{-1}$)	0.639	0.527	0.758	0.935
I_s (mag)	18.127	18.123	18.171	18.180
	0.017	0.020	0.015	0.012
I_b (mag)	18.563	18.571	18.501	18.489
	0.026	0.030	0.020	0.016
H_s (mag)	15.871	15.867	15.915	15.924
	0.023	0.026	0.022	0.020
χ^2_{lc}	15212.20	15214.92	15204.70	15204.43
$\Delta\chi^2_{kep}$	0.00	0.00	0.00	0.00
$\Delta\chi^2_{kin}$	0.00	0.00	0.00	0.00
$\Delta\chi^2_{gal}$	0.00	0.00	0.00	0.00
χ^2	15212.20	15214.92	15204.70	15204.43
dof	15211	15211	15211	15211

Note. — Notation is the same as for Table 2.

Table 5. Model Parameters. Full keplerian orbit with keplerian prior (K_p).

Parameter	M-dwarf		high-mass brown dwarf		low-mass brown dwarf	
	P ₊₋ K _p	P ₋₊ K _p	P ₊₋ K _p	P ₋₊ K _p	P ₊₊ K _p	P ₋₋ K _p
t_0 (HJD')	6573.051	6573.052	6573.050	6573.049	6573.053	6573.053
	0.009	0.009	0.009	0.009	0.008	0.009
t_E (days)	19.93	19.93	20.01	20.08	20.38	20.63
	0.27	0.19	0.31	0.26	0.19	0.16
u_0 (10^{-2})	7.942	-7.944	7.862	-7.816	7.816	-7.687
	0.165	0.120	0.177	0.150	0.134	0.080
q (10^{-4})	3.420	3.330	3.436	3.401	3.838	4.010
	0.165	0.118	0.132	0.160	0.185	0.155
s_0	2.387	2.374	2.374	2.375	2.402	2.403
	0.016	0.009	0.025	0.017	0.013	0.028
α_0 (radian)	3.1311	3.1540	3.1335	3.1540	2.9711	3.3154
	0.0049	0.0048	0.0068	0.0037	0.0065	0.0042
ρ (10^{-3})	3.88	3.81	3.84	3.82	4.05	4.09
	0.13	0.11	0.10	0.12	0.12	0.10
$\pi_{E,N}$	-0.005	0.030	-0.768	0.758	2.256	-2.244
	0.050	0.040	0.177	0.118	0.104	0.117
$\pi_{E,E}$	-0.232	-0.216	-0.256	-0.225	-0.107	-0.221
	0.085	0.075	0.090	0.084	0.090	0.070
π_E	0.232	0.218	0.809	0.790	2.259	2.255
	0.086	0.072	0.147	0.104	0.103	0.115
ω (rad yr $^{-1}$)	0.295	-0.256	-0.475	0.506	1.074	-1.031
	0.030	0.012	0.121	0.137	0.047	0.090
ds/dt (yr $^{-1}$)	-0.001	-0.109	-0.122	-0.001	0.005	0.072
	0.011	0.144	0.222	0.049	0.046	0.295
s_z	0.365	1.458	1.031	0.027	0.098	0.256
	0.613	0.782	1.006	0.110	0.076	0.484
ds_z/dt (yr $^{-1}$)	0.008	0.178	0.281	0.067	-0.100	-0.659
	0.066	0.319	0.516	0.629	0.405	0.875
I_s (mag)	18.115	18.115	18.126	18.132	18.133	18.151
	0.021	0.015	0.023	0.019	0.016	0.011
I_b (mag)	18.583	18.583	18.565	18.556	18.556	18.529
	0.032	0.023	0.035	0.029	0.023	0.016
H_s (mag)	15.859	15.859	15.870	15.876	15.877	15.895
	0.026	0.022	0.028	0.025	0.022	0.019
χ^2_{Ic}	15218.11	15218.29	15215.84	15217.62	15210.27	15207.90
$\Delta\chi^2_{kep}$	-66.30	-66.44	-61.96	-62.08	-55.91	-55.95
$\Delta\chi^2_{kin}$	0.00	0.00	0.00	0.00	0.00	0.00
$\Delta\chi^2_{gal}$	0.00	0.00	0.00	0.00	0.00	0.00
χ^2	15151.81	15151.85	15153.88	15155.54	15154.35	15151.95
dof	15211	15211	15211	15211	15211	15211

Note. — Notation is the same as for Table 2.

Table 6. Model Parameters. Kepler prior + kinematic constraint (K_{pk})

Parameter	M-dwarf		high-mass brown dwarf		low-mass brown dwarf	
	P ₊₋ K _{pk}	P ₋₊ K _{pk}	P ₊₋ K _{pk}	P ₋₊ K _{pk}	P ₊₊ K _{pk}	P ₋₋ K _{pk}
t_0 (HJD')	6573.047	6573.054	6573.050	6573.051	6573.052	6573.054
	0.009	0.009	0.009	0.008	0.009	0.010
t_E (days)	20.20	19.83	19.96	19.93	20.41	20.52
	0.16	0.23	0.10	0.24	0.32	0.28
u_0 (10^{-2})	7.797	-7.960	7.890	-7.905	7.804	-7.749
	0.119	0.147	0.072	0.153	0.187	0.154
q (10^{-4})	3.526	3.124	3.557	3.400	3.812	4.054
	0.176	0.120	0.131	0.158	0.189	0.279
s_0	2.388	2.344	2.394	2.382	2.396	2.407
	0.018	0.012	0.011	0.021	0.015	0.014
α_0 (radian)	3.1269	3.1568	3.1381	3.1516	2.9719	3.3182
	0.0073	0.0058	0.0027	0.0059	0.0103	0.0102
ρ (10^{-3})	3.89	3.72	3.92	3.85	4.03	4.13
	0.13	0.08	0.11	0.13	0.13	0.16
$\pi_{E,N}$	0.047	0.289	-0.891	0.793	2.242	-2.308
	0.098	0.068	0.070	0.074	0.245	0.212
$\pi_{E,E}$	-0.315	-0.118	-0.259	-0.191	-0.108	-0.190
	0.057	0.103	0.059	0.076	0.117	0.108
π_E	0.319	0.312	0.928	0.815	2.245	2.316
	0.062	0.072	0.067	0.076	0.241	0.213
ω (rad yr $^{-1}$)	0.302	0.040	-0.552	0.512	1.074	-1.065
	0.036	0.030	0.065	0.069	0.162	0.141
ds/dt (yr $^{-1}$)	0.047	-0.304	0.002	0.001	-0.001	0.049
s_z	0.076	0.185	0.057	0.083	0.035	0.119
	1.197	1.078	0.149	0.003	0.023	0.243
ds_z/dt (yr $^{-1}$)	1.126	0.732	0.370	0.019	0.212	0.564
	-0.095	0.658	-0.048	0.084	0.192	-0.493
I_s (mag)	0.185	0.112	0.406	0.423	0.995	0.908
	18.135	18.112	18.122	18.120	18.135	18.142
I_b (mag)	0.014	0.018	0.007	0.019	0.025	0.020
	18.552	18.588	18.571	18.574	18.552	18.542
H_s (mag)	0.020	0.028	0.011	0.029	0.036	0.029
	15.879	15.856	15.866	15.864	15.879	15.886
	0.021	0.024	0.018	0.025	0.030	0.026
χ^2_{lc}	15218.49	15220.05	15215.31	15217.48	15210.26	15207.67
$\Delta\chi^2_{\text{kep}}$	-65.62	-65.73	-61.27	-61.93	-55.94	-55.80
$\Delta\chi^2_{\text{kin}}$	13.53	5.89	7.81	4.03	1.91	1.88
$\Delta\chi^2_{\text{gal}}$	0.00	0.00	0.00	0.00	0.00	0.00
χ^2	15166.40	15160.20	15161.85	15159.58	15156.24	15153.75
dof	15211	15211	15211	15211	15211	15211

Note. — Notation is the same as for Table 2.

Table 7. Model Parameters. Keplerian prior + kinematic+Galactic prior (K_{pkg})

Parameter	M-dwarf		high-mass brown dwarf				low-mass brown dwarf	
	P ₊₋ K _{pkg}	P ₋₊ K _{pkg}	P ₊₋ K _{pkg}	P ₋₊ K _{pkg}	P ₊₊ K _{pkg}	P ₋₋ K _{pkg}	P ₊₊ K _{pkg}	P ₋₋ K _{pkg}
t_0 (HJD')	6573.048	6573.055	6573.051	6573.052	6573.052	6573.051	6573.052	6573.052
	0.009	0.009	0.009	0.009	0.009	0.009	0.008	0.008
t_E (days)	20.14	19.70	20.01	19.88	19.96	20.09	20.43	20.64
	0.21	0.25	0.29	0.28	0.26	0.22	0.30	0.25
u_0 (10^{-2})	7.796	-8.042	7.860	-7.919	7.956	-7.897	7.778	-7.672
	0.104	0.162	0.172	0.165	0.159	0.130	0.160	0.140
q (10^{-4})	3.514	3.137	3.436	3.364	3.379	3.307	3.754	3.969
	0.070	0.082	0.146	0.155	0.203	0.196	0.240	0.274
s_0	2.388	2.349	2.373	2.381	2.382	2.339	2.390	2.399
	0.007	0.016	0.016	0.015	0.021	0.037	0.042	0.019
α_0 (radian)	3.1253	3.1563	3.1337	3.1528	2.9868	3.2979	2.9750	3.3119
	0.0052	0.0063	0.0066	0.0068	0.0054	0.0057	0.0062	0.0103
ρ (10^{-3})	3.88	3.75	3.84	3.84	3.86	3.79	3.99	4.06
	0.08	0.09	0.12	0.10	0.15	0.13	0.15	0.16
$\pi_{E,N}$	0.062	0.278	-0.768	0.755	0.785	-0.836	2.200	-2.201
	0.069	0.063	0.142	0.112	0.042	0.114	0.110	0.168
$\pi_{E,E}$	-0.288	-0.087	-0.256	-0.166	-0.166	-0.241	-0.098	-0.211
	0.069	0.076	0.090	0.098	0.097	0.093	0.088	0.092
π_E	0.295	0.291	0.810	0.773	0.802	0.870	2.202	2.211
	0.072	0.059	0.138	0.110	0.049	0.115	0.108	0.169
ω (rad yr $^{-1}$)	0.303	0.019	-0.474	0.485	-0.299	0.268	1.065	-1.025
	0.034	0.011	0.101	0.050	0.071	0.072	0.076	0.067
ds/dt (yr $^{-1}$)	0.033	-0.299	-0.120	-0.006	-0.082	-0.508	-0.006	0.087
	0.020	0.075	0.028	0.039	0.053	0.417	0.470	0.069
s_z	0.840	1.086	1.128	0.054	0.199	1.335	0.084	0.374
	0.629	0.907	1.291	0.078	0.103	0.756	0.180	0.496
ds_z/dt (yr $^{-1}$)	-0.093	0.648	0.255	0.256	0.972	0.891	0.108	-0.562
	0.188	0.238	0.324	0.371	0.203	0.548	0.923	0.674
I_s (mag)	18.133	18.101	18.127	18.118	18.113	18.121	18.138	18.153
	0.014	0.020	0.022	0.022	0.021	0.017	0.022	0.019
I_b (mag)	18.555	18.605	18.565	18.578	18.586	18.573	18.548	18.526
	0.021	0.032	0.033	0.033	0.032	0.025	0.032	0.026
H_s (mag)	15.877	15.845	15.871	15.862	15.857	15.865	15.882	15.897
	0.021	0.026	0.027	0.027	0.026	0.023	0.027	0.025
χ^2_{lc}	15219.03	15220.81	15215.83	15217.93	15217.85	15215.74	15210.37	15208.07
$\Delta\chi^2_{\text{kep}}$	-65.82	-65.90	-61.96	-62.20	-62.01	-61.58	-56.04	-56.06
$\Delta\chi^2_{\text{kin}}$	13.41	5.14	9.06	3.95	3.82	8.35	1.93	2.02
$\Delta\chi^2_{\text{gal}}$	-38.35	-38.70	-30.50	-30.95	-30.60	-29.89	-21.33	-21.20
χ^2	15128.27	15121.36	15132.43	15128.74	15129.06	15132.64	15134.94	15132.83
dof	15211	15211	15211	15211	15211	15211	15211	15211

Note. — Notation is the same as for Table 2.

Table 8. Lens physical parameters (Parallax only).

Parameter	P ₊₋	P ₋₊	P ₊₊	P ₋₋
θ_E (mas)	0.482 ± 0.036	0.486 ± 0.036	0.478 ± 0.036	0.474 ± 0.035
μ_{geo} (mas yr ⁻¹)	8.61 ± 0.67	8.63 ± 0.67	8.47 ± 0.66	8.38 ± 0.64
$\mu_{\text{hel,N}}$ (mas yr ⁻¹)	-6.83 ± 0.52	6.19 ± 0.49	7.98 ± 0.65	-8.54 ± 0.63
$\mu_{\text{hel,E}}$ (mas yr ⁻¹)	-5.73 ± 0.42	-6.22 ± 0.46	-2.51 ± 0.12	-2.75 ± 0.14
D_l (kpc)	$3.14^{+0.44}_{-0.48}$	$3.22^{+0.43}_{-0.49}$	$1.50^{+0.15}_{-0.10}$	$1.47^{+0.14}_{-0.10}$
M_h (M_\odot)	$0.147^{+0.031}_{-0.037}$	$0.156^{+0.030}_{-0.040}$	$0.052^{+0.008}_{-0.005}$	$0.050^{+0.007}_{-0.005}$
M_p (M_\oplus)	$16.99^{+2.99}_{-3.59}$	$17.83^{+2.93}_{-3.87}$	$6.09^{+0.83}_{-0.45}$	$5.98^{+0.75}_{-0.44}$
a_\perp (AU)	$3.62^{+0.51}_{-0.60}$	$3.73^{+0.50}_{-0.61}$	$1.71^{+0.15}_{-0.10}$	$1.67^{+0.13}_{-0.11}$
a_\perp/a_{snow}	$9.10^{+1.59}_{-0.83}$	$8.85^{+1.61}_{-0.76}$	$12.28^{+0.77}_{-0.78}$	$12.44^{+0.83}_{-0.67}$
a_{exp} (AU)	$4.43^{+0.62}_{-0.73}$	$4.57^{+0.61}_{-0.75}$	$2.10^{+0.18}_{-0.12}$	$2.04^{+0.16}_{-0.13}$
$a_{\text{exp}}/a_{\text{snow}}$	$11.14^{+1.95}_{-1.01}$	$10.84^{+1.97}_{-0.93}$	$15.04^{+0.94}_{-0.95}$	$15.24^{+1.01}_{-0.82}$
$\tilde{v}_{t,l}$ (km s ⁻¹)	-208.5 ± 35.3	71.7 ± 34.9	63.1 ± 4.9	-64.7 ± 4.8
$\tilde{v}_{t,b}$ (km s ⁻¹)	46.7 ± 31.7	228.9 ± 33.8	62.2 ± 3.0	-9.3 ± 2.9
$T_{\text{eff,exp}}$ (K)	20^{+5}_{-7}	21^{+5}_{-7}	10^{+1}_{-3}	10^{+1}_{-3}

Note. — $a_{\text{exp}} = \sqrt{3/2}a_\perp$ is an expected 3D separation for the measured projected separation, a_\perp . $a_{\text{snow}} = 2.7(M_h/M_\odot)$ is the snow-line. $T_{\text{eff,exp}}$ is the effective temperature of the planet when it was formed based on the M_h and a_{exp} .

Table 9. Lens physical parameters. Linear orbit (L)

Parameter	P _{+-L}	P _{-+L}	P _{++L}	P _{--L}
θ_E (mas)	0.475±0.034	0.485±0.039	0.460±0.037	0.424±0.035
μ_{geo} (mas yr ⁻¹)	8.48± 0.63	8.69± 0.72	7.69± 0.64	7.11± 0.61
$\mu_{\text{hel,N}}$ (mas yr ⁻¹)	-8.83± 0.63	8.17± 0.72	6.61± 0.64	-7.99± 0.61
$\mu_{\text{hel,E}}$ (mas yr ⁻¹)	-2.59± 0.10	-2.37± 0.10	-2.84± 0.01	-2.77± 0.03
D_l (kpc)	1.16 ^{+0.12} _{-0.17}	1.22 ^{+0.40} _{-0.04}	0.54 ^{+0.06} _{-0.05}	0.64 ^{+0.08} _{-0.05}
M_h (M_\odot)	0.038 ^{+0.004} _{-0.006}	0.042 ^{+0.015} _{-0.003}	0.015 ^{+0.002} _{-0.000}	0.015 ^{+0.005} _{-0.001}
M_p (M_\oplus)	4.54 ^{+0.55} _{-0.74}	4.74 ^{+1.79} _{-0.21}	2.11 ^{+0.23} _{-0.23}	2.53 ^{+0.36} _{-0.24}
a_\perp (AU)	1.31 ^{+0.11} _{-0.19}	1.39 ^{+0.43} _{-0.05}	0.58 ^{+0.05} _{-0.05}	0.67 ^{+0.11} _{-0.04}
a_\perp/a_{snow}	12.87 ^{+0.63} _{-0.46}	12.40 ^{+1.17} _{-0.73}	14.08 ^{+0.51} _{-1.73}	16.05 ^{+0.24} _{-2.15}
a_{exp} (AU)	1.60 ^{+0.13} _{-0.23}	1.70 ^{+0.53} _{-0.06}	0.70 ^{+0.06} _{-0.06}	0.82 ^{+0.13} _{-0.05}
$a_{\text{exp}}/a_{\text{snow}}$	15.76 ^{+0.77} _{-0.56}	15.19 ^{+1.43} _{-0.90}	17.24 ^{+0.62} _{-2.12}	19.66 ^{+0.30} _{-2.63}
$\tilde{v}_{t,l}$ (km s ⁻¹)	-47.1± 6.1	53.5± 8.2	24.4± 1.1	-16.1± 2.1
$\tilde{v}_{t,b}$ (km s ⁻¹)	-7.2± 3.6	49.8± 4.8	23.3± 0.6	1.7± 1.2
$T_{\text{eff,exp}}$ (K)	9 ⁺¹ ₋₃	9 ⁺² ₋₃	5 ⁺¹ ₋₁	5 ⁺¹ ₋₁
KE/PE _⊥	1.000	0.994	0.988	0.964

Note. — Notation is the same as for Table 8.

Table 10. Lens physical parameters. Keplerian orbit (K)

Parameter	P ₊₋ K	P ₋₊ K	P ₊₊ K	P ₋₋ K
θ_E (mas)	0.464 \pm 0.032	0.469 \pm 0.034	0.454 \pm 0.035	0.410 \pm 0.031
μ_{geo} (mas yr ⁻¹)	8.28 \pm 0.60	8.40 \pm 0.63	7.70 \pm 0.61	6.91 \pm 0.54
$\mu_{\text{hel,N}}$ (mas yr ⁻¹)	-8.61 \pm 0.59	7.90 \pm 0.62	6.73 \pm 0.61	-7.76 \pm 0.54
$\mu_{\text{hel,E}}$ (mas yr ⁻¹)	-2.59 \pm 0.10	-2.31 \pm 0.09	-2.60 \pm 0.01	-2.62 \pm 0.02
D_l (kpc)	1.20 $^{+0.39}_{-0.03}$	1.26 $^{+0.27}_{-0.08}$	0.60 $^{+0.06}_{-0.05}$	0.67 $^{+0.07}_{-0.05}$
M_h (M_\odot)	0.037 $^{+0.014}_{-0.001}$	0.040 $^{+0.010}_{-0.004}$	0.016 $^{+0.003}_{-0.001}$	0.015 $^{+0.002}_{-0.001}$
M_p (M_\oplus)	4.70 $^{+1.69}_{-0.16}$	4.93 $^{+1.37}_{-0.23}$	2.31 $^{+0.28}_{-0.16}$	2.60 $^{+0.35}_{-0.17}$
a_\perp (AU)	1.35 $^{+0.40}_{-0.03}$	1.43 $^{+0.28}_{-0.08}$	0.65 $^{+0.04}_{-0.04}$	0.69 $^{+0.05}_{-0.04}$
a_\perp/a_{snow}	13.39 $^{+0.51}_{-0.77}$	13.10 $^{+0.92}_{-0.53}$	14.72 $^{+0.53}_{-1.22}$	17.10 $^{+0.47}_{-1.29}$
a_{exp} (AU)	1.65 $^{+0.49}_{-0.04}$	1.75 $^{+0.34}_{-0.09}$	0.80 $^{+0.05}_{-0.05}$	0.85 $^{+0.06}_{-0.05}$
$a_{\text{exp}}/a_{\text{snow}}$	16.40 $^{+0.63}_{-0.94}$	16.05 $^{+1.13}_{-0.65}$	18.03 $^{+0.64}_{-1.50}$	20.95 $^{+0.58}_{-1.58}$
a_{kep} (AU)	114 $^{+0}_{-112}$	117 $^{+0}_{-113}$	49 $^{+0}_{-44}$	44 $^{+0}_{-41}$
$a_{\text{kep}}/a_{\text{snow}}$	1134 $^{+0}_{-1116}$	1069 $^{+0}_{-1035}$	1092 $^{+0}_{-1006}$	1080 $^{+0}_{-1022}$
P (yr)	6304 $^{+0}_{-6280}$	6260 $^{+0}_{-6217}$	2635 $^{+0}_{-2572}$	2362 $^{+0}_{-2331}$
e	0.99 $^{+0.00}_{-0.52}$	0.99 $^{+0.00}_{-0.32}$	0.99 $^{+0.00}_{-0.15}$	0.98 $^{+0.00}_{-0.25}$
i	177.7 $^{+0.0}_{-21.9}$	0.7 $^{+22.5}_{-0.0}$	4.7 $^{+7.8}_{-1.2}$	161.6 $^{+8.5}_{-4.6}$
$\tilde{v}_{t,l}$ (km s ⁻¹)	-47.8 \pm 7.0	53.6 \pm 6.7	26.5 \pm 1.4	-16.3 \pm 1.2
$\tilde{v}_{t,b}$ (km s ⁻¹)	-6.9 \pm 4.2	50.1 \pm 3.9	24.7 \pm 0.8	1.4 \pm 0.7
$T_{\text{eff,kep}}$ (K)	1.0 $^{+0.5}_{-0.6}$	1.1 $^{+0.5}_{-0.5}$	0.7 $^{+0.3}_{-0.2}$	0.7 $^{+0.3}_{-0.3}$
KE/PE _⊥	0.992	0.994	0.987	0.944
KE/PE	0.994	0.994	0.993	0.992

Note. — Notation is the same as for Table 8, except $T_{\text{eff,kep}}$ is based on a_{kep} . When the best fit is larger or smaller than the 68% confidence interval of MCMC chains, the upper or lower limit is designated as “+0.0” or “−0.0”, respectively.

Table 11. Lens physical parameters. Keplerian orbit with Keplerian prior (K_p)

Parameter	M-dwarf		high-mass brown dwarf		low-mass brown dwarf	
	P ₊ –K _p	P _– +K _p	P ₊ –K _p	P _– +K _p	P ₊₊ K _p	P _– –K _p
θ_E (mas)	0.482±0.035	0.491±0.034	0.487±0.034	0.489±0.035	0.462±0.033	0.458±0.031
μ_{geo} (mas yr ^{−1})	8.62± 0.65	8.78± 0.63	8.66± 0.63	8.68± 0.64	8.07± 0.59	7.90± 0.56
$\mu_{\text{hel,N}}$ (mas yr ^{−1})	−0.27± 0.02	1.13± 0.09	−8.47± 0.60	8.08± 0.62	7.41± 0.59	−8.51± 0.56
$\mu_{\text{hel,E}}$ (mas yr ^{−1})	−8.81± 0.65	−8.88± 0.63	−3.43± 0.20	−3.14± 0.18	−2.19± 0.03	−2.57± 0.05
D_l (kpc)	4.22 ^{+0.63} _{−0.97}	4.31 ^{+0.80} _{−0.78}	1.93 ^{+0.40} _{−0.23}	1.95 ^{+0.45} _{−0.11}	0.86 ^{+0.07} _{−0.06}	0.86 ^{+0.04} _{−0.09}
M_h (M_\odot)	0.256 ^{+0.061} _{−0.094}	0.276 ^{+0.095} _{−0.083}	0.074 ^{+0.020} _{−0.012}	0.076 ^{+0.018} _{−0.007}	0.025 ^{+0.003} _{−0.002}	0.025 ^{+0.002} _{−0.003}
M_p (M_\oplus)	29.13 ^{+6.53} _{−9.98}	30.68 ^{+10.12} _{−8.71}	8.45 ^{+2.37} _{−1.18}	8.62 ^{+2.61} _{−0.44}	3.21 ^{+0.30} _{−0.27}	3.33 ^{+0.19} _{−0.40}
a_\perp (AU)	4.86 ^{+0.75} _{−1.12}	5.02 ^{+0.94} _{−0.92}	2.23 ^{+0.42} _{−0.26}	2.27 ^{+0.43} _{−0.13}	0.95 ^{+0.04} _{−0.04}	0.95 ^{+0.01} _{−0.09}
a_\perp/a_{snow}	7.05 ^{+2.12} _{−0.86}	6.73 ^{+1.72} _{−1.14}	11.17 ^{+0.99} _{−0.79}	11.07 ^{+0.80} _{−0.59}	14.02 ^{+0.62} _{−0.53}	14.13 ^{+0.64} _{−0.38}
a_{exp} (AU)	5.95 ^{+0.92} _{−1.38}	6.15 ^{+1.15} _{−1.13}	2.73 ^{+0.51} _{−0.31}	2.78 ^{+0.53} _{−0.16}	1.16 ^{+0.05} _{−0.05}	1.16 ^{+0.01} _{−0.11}
$a_{\text{exp}}/a_{\text{snow}}$	8.63 ^{+2.59} _{−1.05}	8.24 ^{+2.10} _{−1.40}	13.69 ^{+1.21} _{−0.97}	13.55 ^{+0.98} _{−0.72}	17.17 ^{+0.75} _{−0.66}	17.31 ^{+0.78} _{−0.47}
a_{kep} (AU)	4.92 ^{+1.72} _{−0.75}	5.90 ^{+6.10} _{−1.30}	2.43 ^{+3.49} _{−0.19}	2.27 ^{+0.88} _{−0.22}	0.95 ^{+0.09} _{−0.03}	0.96 ^{+0.72} _{−0.01}
$a_{\text{kep}}/a_{\text{snow}}$	7.14 ^{+4.70} _{−0.77}	7.90 ^{+9.22} _{−1.66}	12.18 ^{+17.62} _{−1.22}	11.08 ^{+3.86} _{−1.86}	14.02 ^{+1.67} _{−0.50}	14.21 ^{+12.66} _{−0.00}
P (yr)	21.6 ^{+11.7} _{−1.8}	27.2 ^{+51.5} _{−7.1}	13.9 ^{+38.6} _{−1.6}	12.4 ^{+7.1} _{−2.0}	5.8 ^{+0.8} _{−0.2}	5.9 ^{+8.3} _{−0.0}
e	0.00 ^{+0.24} _{−0.00}	0.00 ^{+0.59} _{−0.00}	0.00 ^{+0.62} _{−0.00}	0.00 ^{+0.43} _{−0.00}	0.00 ^{+0.09} _{−0.00}	0.00 ^{+0.45} _{−0.00}
i	8.7 ^{+23.7} _{−0.8}	143.7 ^{+9.6} _{−13.2}	152.3 ^{+4.0} _{−24.4}	3.2 ^{+49.0} _{−0.0}	3.2 ^{+9.8} _{−0.0}	163.9 ^{+3.8} _{−18.9}
$\tilde{v}_{t,l}$ (km s ^{−1})	−188.7± 69.3	−144.1± 67.2	−99.5± 16.3	80.7± 12.2	37.0± 1.5	−28.6± 1.7
$\tilde{v}_{t,b}$ (km s ^{−1})	333.8±120.8	382.3±114.3	−8.2± 10.6	91.8± 7.8	33.1± 0.9	−2.4± 1.0
$T_{\text{eff,kep}}$ (K)	33 ⁺¹² _{−10}	33 ⁺¹⁰ _{−20}	14 ⁺² _{−10}	15 ⁺¹ _{−4}	7 ⁺¹ _{−1}	7 ⁺¹ _{−3}
KE/PE _⊥	0.495	0.394	0.432	0.499	0.498	0.464
KE/PE	0.500	0.500	0.500	0.500	0.500	0.500

Note. — Notation is the same as for Table 10.

Table 12. Lens physical parameters. Keplerian prior + kinematic constraint (K_{pk})

Parameter	M-dwarf		high-mass brown dwarf		low-mass brown dwarf	
	$P_{+-}K_{\text{pk}}$	$P_{-+}K_{\text{pk}}$	$P_{+-}K_{\text{pk}}$	$P_{-+}K_{\text{pk}}$	$P_{++}K_{\text{pk}}$	$P_{--}K_{\text{pk}}$
θ_E (mas)	0.481 ± 0.035	0.503 ± 0.034	0.477 ± 0.033	0.486 ± 0.035	0.464 ± 0.033	0.452 ± 0.034
μ_{geo} (mas yr $^{-1}$)	8.48 ± 0.63	9.03 ± 0.63	8.51 ± 0.61	8.68 ± 0.65	8.11 ± 0.61	7.86 ± 0.61
$\mu_{\text{hel,N}}$ (mas yr $^{-1}$)	1.16 ± 0.09	8.26 ± 0.59	-8.45 ± 0.59	8.19 ± 0.63	7.44 ± 0.61	-8.48 ± 0.61
$\mu_{\text{hel,E}}$ (mas yr $^{-1}$)	-8.65 ± 0.63	-3.69 ± 0.24	-3.14 ± 0.17	-2.72 ± 0.15	-2.20 ± 0.03	-2.47 ± 0.05
D_l (kpc)	$3.59^{+0.60}_{-0.39}$	$3.55^{+0.20}_{-0.78}$	$1.76^{+0.19}_{-0.15}$	$1.92^{+0.28}_{-0.12}$	$0.86^{+0.12}_{-0.06}$	$0.85^{+0.08}_{-0.08}$
M_h (M_\odot)	$0.185^{+0.054}_{-0.034}$	$0.198^{+0.007}_{-0.065}$	$0.063^{+0.006}_{-0.006}$	$0.073^{+0.014}_{-0.006}$	$0.025^{+0.004}_{-0.003}$	$0.024^{+0.004}_{-0.003}$
M_p (M_\oplus)	$21.77^{+5.31}_{-3.34}$	$20.58^{+0.56}_{-6.66}$	$7.47^{+0.87}_{-0.77}$	$8.28^{+1.35}_{-0.67}$	$3.23^{+0.55}_{-0.29}$	$3.24^{+0.38}_{-0.30}$
a_\perp (AU)	$4.13^{+0.74}_{-0.48}$	$4.18^{+0.23}_{-0.96}$	$2.01^{+0.15}_{-0.14}$	$2.22^{+0.29}_{-0.12}$	$0.95^{+0.11}_{-0.08}$	$0.93^{+0.08}_{-0.08}$
a_\perp/a_{snow}	$8.25^{+1.26}_{-1.09}$	$7.83^{+1.79}_{-0.20}$	$11.82^{+0.70}_{-0.44}$	$11.25^{+0.76}_{-0.72}$	$13.90^{+0.90}_{-0.44}$	$14.34^{+0.73}_{-0.75}$
a_{exp} (AU)	$5.06^{+0.91}_{-0.59}$	$5.12^{+0.29}_{-1.17}$	$2.46^{+0.19}_{-0.17}$	$2.72^{+0.35}_{-0.15}$	$1.17^{+0.14}_{-0.09}$	$1.14^{+0.09}_{-0.09}$
$a_{\text{exp}}/a_{\text{snow}}$	$10.11^{+1.55}_{-1.34}$	$9.59^{+2.20}_{-0.24}$	$14.47^{+0.86}_{-0.54}$	$13.78^{+0.93}_{-0.88}$	$17.02^{+1.10}_{-0.54}$	$17.57^{+0.89}_{-0.91}$
a_{kep} (AU)	$4.62^{+4.71}_{-0.71}$	$4.60^{+2.66}_{-1.18}$	$2.01^{+1.10}_{-0.04}$	$2.22^{+0.84}_{-0.17}$	$0.95^{+0.32}_{-0.03}$	$0.93^{+0.68}_{-0.01}$
$a_{\text{kep}}/a_{\text{snow}}$	$9.23^{+10.23}_{-1.47}$	$8.63^{+7.94}_{-1.08}$	$11.83^{+7.08}_{-0.33}$	$11.26^{+3.37}_{-0.93}$	$13.90^{+5.58}_{-0.78}$	$14.42^{+10.92}_{-0.00}$
P (yr)	$23.0^{+42.8}_{-4.5}$	$22.2^{+24.9}_{-6.1}$	$11.4^{+10.7}_{-0.3}$	$12.2^{+6.7}_{-1.1}$	$5.8^{+3.1}_{-0.2}$	$5.8^{+7.4}_{-0.0}$
e	$0.00^{+0.48}_{-0.00}$	$0.00^{+0.51}_{-0.00}$	$0.00^{+0.38}_{-0.00}$	$0.00^{+0.27}_{-0.00}$	$0.00^{+0.30}_{-0.00}$	$0.00^{+0.41}_{-0.00}$
i	$27.8^{+20.4}_{-13.1}$	$83.4^{+4.1}_{-4.4}$	$175.9^{+0.0}_{-27.0}$	$3.9^{+34.0}_{-0.0}$	$4.3^{+28.4}_{-0.0}$	$167.7^{+0.0}_{-23.8}$
$\tilde{v}_{t,l}$ (km s $^{-1}$)	-92.4 ± 26.5	177.3 ± 53.3	-85.5 ± 5.7	82.8 ± 8.6	37.2 ± 3.6	-27.7 ± 2.9
$\tilde{v}_{t,b}$ (km s $^{-1}$)	263.4 ± 44.8	233.3 ± 36.5	-9.2 ± 3.6	86.1 ± 5.3	33.2 ± 2.0	-2.6 ± 1.7
$T_{\text{eff,kep}}$ (K)	25^{+5}_{-15}	27^{+9}_{-8}	13^{+1}_{-4}	14^{+1}_{-4}	7^{+1}_{-2}	7^{+1}_{-3}
KE/PE $_\perp$	0.439	0.086	0.498	0.498	0.497	0.480
KE/PE	0.500	0.500	0.500	0.500	0.500	0.500

Note. — Notation is the same as for Table 10.

Table 13. Lens physical parameters. Keplerian prior + kinematic + Galactic density prior (K_{pkg})

Parameter	M-dwarf		high-mass brown dwarf				low-mass brown dwarf	
	$P_{+-}K_{\text{pkg}}$	$P_{-+}K_{\text{pkg}}$	$P_{+-}K_{\text{pkg}}$	$P_{-+}K_{\text{pkg}}$	$P_{++}K_{\text{pkg}}$	$P_{--}K_{\text{pkg}}$	$P_{++}K_{\text{pkg}}$	$P_{--}K_{\text{pkg}}$
θ_E (mas)	0.482 ± 0.033	0.498 ± 0.034	0.487 ± 0.035	0.487 ± 0.034	0.485 ± 0.036	0.493 ± 0.036	0.469 ± 0.035	0.461 ± 0.035
μ_{geo} (mas yr $^{-1}$)	8.53 ± 0.60	9.01 ± 0.64	8.66 ± 0.65	8.72 ± 0.63	8.65 ± 0.67	8.74 ± 0.66	8.17 ± 0.63	7.96 ± 0.62
$\mu_{\text{hel,N}}$ (mas yr $^{-1}$)	1.71 ± 0.13	8.51 ± 0.61	-8.47 ± 0.61	8.28 ± 0.62	8.22 ± 0.66	-8.67 ± 0.63	7.52 ± 0.63	-8.56 ± 0.62
$\mu_{\text{hel,E}}$ (mas yr $^{-1}$)	-8.59 ± 0.59	-2.96 ± 0.19	-3.42 ± 0.20	-2.53 ± 0.14	-2.47 ± 0.14	-3.17 ± 0.18	-2.16 ± 0.03	-2.53 ± 0.06
D_l (kpc)	$3.74^{+0.68}_{-0.55}$	$3.70^{+0.49}_{-0.55}$	$1.93^{+0.38}_{-0.19}$	$2.00^{+0.20}_{-0.26}$	$1.95^{+0.16}_{-0.16}$	$1.81^{+0.38}_{-0.08}$	$0.86^{+0.10}_{-0.04}$	$0.87^{+0.07}_{-0.08}$
M_h (M_\odot)	$0.201^{+0.053}_{-0.045}$	$0.210^{+0.033}_{-0.050}$	$0.074^{+0.022}_{-0.010}$	$0.077^{+0.009}_{-0.016}$	$0.074^{+0.007}_{-0.009}$	$0.070^{+0.023}_{-0.005}$	$0.026^{+0.005}_{-0.000}$	$0.026^{+0.003}_{-0.004}$
M_p (M_\oplus)	$23.54^{+6.29}_{-5.07}$	$21.96^{+3.84}_{-4.88}$	$8.45^{+2.26}_{-1.04}$	$8.66^{+1.07}_{-1.46}$	$8.35^{+0.75}_{-0.71}$	$7.67^{+2.40}_{-0.28}$	$3.27^{+0.43}_{-0.20}$	$3.39^{+0.29}_{-0.35}$
a_\perp (AU)	$4.31^{+0.72}_{-0.65}$	$4.33^{+0.54}_{-0.66}$	$2.22^{+0.44}_{-0.22}$	$2.31^{+0.19}_{-0.34}$	$2.25^{+0.14}_{-0.17}$	$2.08^{+0.47}_{-0.08}$	$0.97^{+0.08}_{-0.02}$	$0.97^{+0.04}_{-0.08}$
a_\perp/a_{snow}	$7.95^{+1.41}_{-0.99}$	$7.64^{+1.47}_{-0.62}$	$11.17^{+0.82}_{-0.96}$	$11.08^{+1.25}_{-0.40}$	$11.22^{+0.93}_{-0.54}$	$11.09^{+0.71}_{-1.00}$	$13.73^{+0.25}_{-1.26}$	$13.99^{+1.00}_{-0.51}$
a_{exp} (AU)	$5.28^{+0.88}_{-0.79}$	$5.31^{+0.67}_{-0.81}$	$2.72^{+0.54}_{-0.28}$	$2.83^{+0.23}_{-0.41}$	$2.75^{+0.17}_{-0.21}$	$2.55^{+0.58}_{-0.10}$	$1.19^{+0.10}_{-0.02}$	$1.18^{+0.05}_{-0.10}$
$a_{\text{exp}}/a_{\text{snow}}$	$9.73^{+1.72}_{-1.21}$	$9.36^{+1.80}_{-0.76}$	$13.68^{+1.01}_{-1.18}$	$13.57^{+1.53}_{-0.48}$	$13.74^{+1.14}_{-0.66}$	$13.58^{+0.87}_{-1.22}$	$16.81^{+0.31}_{-1.54}$	$17.13^{+1.23}_{-0.62}$
a_{kep} (AU)	$4.57^{+3.03}_{-0.76}$	$4.78^{+3.10}_{-1.75}$	$2.46^{+2.15}_{-0.13}$	$2.31^{+0.38}_{-0.27}$	$2.25^{+0.70}_{-0.27}$	$2.40^{+2.86}_{-0.45}$	$0.97^{+0.64}_{-0.00}$	$0.98^{+0.29}_{-0.06}$
$a_{\text{kep}}/a_{\text{snow}}$	$8.42^{+5.38}_{-1.28}$	$8.43^{+6.10}_{-2.52}$	$12.37^{+9.35}_{-1.19}$	$11.09^{+2.92}_{-0.46}$	$11.26^{+3.72}_{-0.92}$	$12.76^{+12.25}_{-3.20}$	$13.74^{+7.07}_{-0.42}$	$14.16^{+4.96}_{-0.21}$
P (yr)	$21.8^{+22.4}_{-3.6}$	$22.8^{+25.3}_{-10.4}$	$14.2^{+20.0}_{-1.2}$	$12.7^{+2.9}_{-1.2}$	$12.4^{+6.1}_{-1.7}$	$14.1^{+28.5}_{-4.0}$	$5.9^{+6.1}_{-0.0}$	$6.0^{+2.9}_{-0.3}$
e	$0.00^{+0.37}_{-0.00}$	$0.00^{+0.83}_{-0.00}$	$0.00^{+0.40}_{-0.00}$	$0.00^{+0.16}_{-0.00}$	$0.00^{+0.31}_{-0.00}$	$0.00^{+0.69}_{-0.00}$	$0.00^{+0.48}_{-0.00}$	$0.00^{+0.19}_{-0.00}$
i	$20.8^{+15.0}_{-6.3}$	$86.7^{+3.0}_{-1.2}$	$151.2^{+4.8}_{-25.1}$	$12.6^{+11.4}_{-7.1}$	$126.0^{+8.0}_{-15.2}$	$63.1^{+4.2}_{-29.4}$	$3.1^{+28.3}_{-0.0}$	$164.3^{+3.5}_{-17.2}$
$\tilde{v}_{t,l}$ (km s $^{-1}$)	-83.2 ± 37.0	210.0 ± 51.7	-99.4 ± 15.3	88.7 ± 13.8	86.0 ± 5.8	-91.0 ± 11.1	37.8 ± 1.7	-29.2 ± 2.5
$\tilde{v}_{t,b}$ (km s $^{-1}$)	290.9 ± 60.9	234.5 ± 33.2	-8.3 ± 10.0	88.6 ± 8.4	84.9 ± 3.5	-10.7 ± 7.0	33.5 ± 1.0	-2.8 ± 1.5
$T_{\text{eff,kep}}$ (K)	27^{+6}_{-11}	28^{+8}_{-10}	14^{+2}_{-7}	15^{+3}_{-2}	14^{+2}_{-3}	13^{+1}_{-9}	8^{+0}_{-3}	7^{+1}_{-1}
KE/PE $_\perp$	0.464	0.081	0.430	0.477	0.175	0.196	0.499	0.470
KE/PE	0.500	0.500	0.500	0.500	0.500	0.500	0.500	0.500

Note. — Notation is the same as for Table 10.